Accepted for Publication in the Astrophysical Journal Supplements, January 4, 2012
Preprint typeset using LaTeX style emulateapj v. 8/13/10

arXiv:1106.3328v3 [astro-ph.CO] 3 Jan 2012

THE CLUSTER LENSING AND SUPERNOVA SURVEY WITH HUBBLE: AN OVERVIEW

Marc Postman[1], Dan Coe[1], Narciso Benítez[2], Larry Bradley[1], Tom Broadhurst[3], Megan Donahue[4], Holland Ford[5], Or Graur[6], Genevieve Graves[7], Stephanie Jouvel[13], Anton Koekemoer[1], Doron Lemze[5], Elinor Medezinski[5], Alberto Molino[2], Leonidas Moustakas[8], Sara Ogaz[1], Adam Riess[1,5], Steve Rodney[5], Piero Rosati[9], Keiichi Umetsu[10], Wei Zheng[5], Adi Zitrin[6], Matthias Bartelmann[11], Rychard Bouwens[12], Nicole Czakon[13], Sunil Golwala[13], Ole Host[14], Leopoldo Infante[15], Saurabh Jha[16], Yolanda Jimenez-Teja[2], Daniel Kelson[17], Ofer Lahav[14], Ruth Lazkoz[3], Dani Maoz[6], Curtis McCully[16], Peter Melchior[18], Massimo Meneghetti[19], Julian Merten[11], John Moustakas[20], Mario Nonino[21], Brandon Patel[16], Enikö Regös[22], Jack Sayers[13], Stella Seitz[23], and Arjen Van der Wel[24]

Accepted for Publication in the Astrophysical Journal Supplements, January 4, 2012

ABSTRACT

The Cluster Lensing And Supernova survey with Hubble (CLASH) is a 524-orbit multi-cycle treasury program to use the gravitational lensing properties of 25 galaxy clusters to accurately constrain their mass distributions. The survey, described in detail in this paper, will definitively establish the degree of concentration of dark matter in the cluster cores, a key prediction of structure formation models. The CLASH cluster sample is larger and less biased than current samples of space-based imaging studies of clusters to similar depth, as we have minimized lensing-based selection that favors systems with overly dense cores. Specifically, twenty CLASH clusters are solely X-ray selected. The X-ray selected clusters are massive ($kT > 5$ keV) and, in most cases, dynamically relaxed. Five additional clusters are included for their lensing strength ($\theta_{Ein} > 35''$ at $z_s = 2$) to optimize the likelihood of finding highly magnified high-z ($z > 7$) galaxies. A total of 16 broadband filters, spanning the near-UV to near-IR, are employed for each 20-orbit campaign on each cluster. These data are used to measure precise ($\sigma_z \sim 0.02(1+z)$) photometric redshifts for newly discovered arcs. Observations of each cluster are spread over 8 epochs to enable a search for Type Ia supernovae at $z > 1$ to improve constraints on the time dependence of the dark energy equation of state and the evolution of supernovae. We present newly re-derived X-ray luminosities, temperatures, and Fe abundances for the CLASH clusters as well as a representative source list for MACS1149.6+2223 ($z = 0.544$).

Subject headings: cosmology: dark matter — cosmology: dark energy — gravitational lensing: strong — gravitational lensing: weak — galaxies: evolution — galaxies: formation

1. INTRODUCTION

The Universe has proven to be far more intriguing in its composition than we knew it to be even just 14 years ago. It is a "dark" Universe where $\sim 23\%$ of its mass-energy density is made up of weakly interacting (and, as yet, undetected) non-baryonic particles (a.k.a. dark matter) and $\sim 73\%$ is as yet unknown physics (a.k.a. dark energy) that is driving an accelerated expansion of the metric (e.g., Komatsu et al. 2010; Riess et al. 2011). The *Hubble Space Telescope* (*HST*) has played a key role in providing evidence for and constraining the nature of both of these mysterious dark components (e.g., Riess et al. 1998; Perlmutter et al. 1999; Clowe et al. 2006).

Clusters of galaxies, by virtue of their position at the high end of the cosmic mass power spectrum, provide a powerful way to constrain the frequency of high amplitude perturbations in the primordial density field. As such, they play a direct and fundamental role in testing cosmological models and in constraining the properties of dark matter (DM), providing unique and independent tests of any viable cosmology and structure formation scenario, and possible modifications of the laws of gravity. A key ingredient of such cluster-based cosmological tests is the mass distribution of clusters, both on (sub) Mpc scales and across the range of populations. The best and highest resolution maps of DM distribution in massive galaxy clusters come from observations of strong gravitational lensing made by the Advanced Camera for Surveys (ACS, Ford et al. 2003) onboard *HST*. As part of a Guaranteed Time Observation (GTO) program, deep (20-orbit) multiband (4-6 filter) observations were obtained for five galaxy clusters: Abell 1689 (Broadhurst et al. 2005; Limousin et al. 2007; Coe et al.

[1] Space Telescope Science Institute, 3700 San Martin Drive, Baltimore, MD 21208, U.S.A.
[2] Instituto de Astrofísica de Andalucía
[3] Department of Theoretical Physics, University of the Basque Country
[4] Michigan State University
[5] The Johns Hopkins University
[6] Tel Aviv University
[7] University of California, Berkeley
[8] The Jet Propulsion Laboratory, California Institute of Technology
[9] European Southern Observatory
[10] Academia Sinica, Institute of Astronomy & Astrophysics
[11] Universitat Heidelberg
[12] Leiden Observatory, Leiden University
[13] California Institute of Technology
[14] University College London
[15] Universidad Catolica de Chile
[16] Rutgers University
[17] The Carnegie Institute for Science; Carnegie Observatories
[18] The Ohio State University
[19] INAF, Osservatorio Astronomico di Bologna
[20] University of California, San Diego
[21] INAF, Osservatorio Astronomico di Trieste
[22] European Laboratory for Particle Physics (CERN)
[23] Universitas Sternwarte, München
[24] Max Planck Institut für Astronomie, Heidelberg

2010); Abell 1703 (Limousin et al. 2008; Saha & Read 2009; Zitrin et al. 2010); Abell 2218 (Elíasdóttir et al. 2007); CL0024+1654 (Jee et al. 2007; Zitrin et al. 2009; Umetsu et al. 2010); and MS1358+6245 (Zitrin et al. 2011c). These results have contributed to a reported tension between observed and simulated galaxy cluster dark matter halos. Observed clusters appear to have denser cores than simulated clusters of similar total (virial) mass (e.g., Broadhurst et al. 2008; Oguri et al. 2009; Sereno et al. 2010). Understanding the true constraints from observed concentration and mass profile measurements on Λ cold dark matter (ΛCDM) structure formation models is one of the important problems that can be tackled with a deep, high angular resolution imaging survey of a significantly larger and more homogeneously selected sample of galaxy clusters.

In May 2009, NASA successfully executed the final planned Hubble Servicing mission, SM4, with the installation of the Wide Field Camera 3 (*WFC3* Kimble et al. 2008) and the repair of *ACS*. Shortly thereafter, the Hubble Multi-Cycle Treasury (MCT) Program was conceived to permit ambitious programs (> 500 orbits) with broad scientific potential that could not be accomplished within the constraints of a single *HST* observing cycle and that would take full advantage of the final era of a newly refurbished *Hubble Space Telescope*.

The Cluster Lensing and Supernova survey with Hubble (CLASH) was one of three MCT programs selected. CLASH has four main science goals:

1. Measure the profiles and substructures of dark matter in galaxy clusters with unprecedented precision and resolution.

2. Detect Type Ia supernovae out to redshift $z \sim 2.5$ to measure the time dependence of the dark energy equation of state and potential evolutionary effects in the supernovae themselves.

3. Detect and characterize some of the most distant galaxies yet discovered at $z > 7$.

4. Study the internal structure and evolution of the galaxies in and behind these clusters.

To accomplish these objectives, the CLASH program targets 25 massive galaxy clusters and will image each in 16 passbands using *WFC3/UVIS*, *WFC3/IR* and *ACS/WFC*. CLASH has been allocated 524 *HST* orbits, spread out over Cycles 18, 19, and 20. The majority of these orbits (474) are for cluster imaging and, simultaneously, for the parallel SN search program. An additional 50 orbits were allocated as a reserve for supernova follow-up observations. Based on a current census of the *HST* data archive, CLASH will produce a six-fold increase the number of lensing clusters observed to a depth of 20 orbits and, more importantly, will vastly increase the number lensing clusters with extensive multi-band *HST* imaging.

Motivations for each of the main CLASH science goals are provided in §2.1, §2.2, §2.3, and §2.4. Subsequent sections describe the cluster sample (§3), survey design (§4), data pipeline (§5), and supporting observations using other facilities (§6). Data products intended for public distribution to the community are briefly described in §7. AB magnitudes are used throughout (Oke 1974). The cosmological parameters $H_o = 100h$ km s^{-1} Mpc^{-1}, $h = 0.7$, $\Omega_m = 0.30$, $\Lambda = 0.70$ are assumed in this paper.

2. SCIENTIFIC MOTIVATION

2.1. *Galaxy Cluster Dark Matter Profiles and Formation Times*

Recent observations suggest that galaxy clusters formed earlier in our universe than in simulated ΛCDM universes. These observations include the detection of perhaps unexpectedly massive galaxy clusters at $z > 1$ (Stanford et al. 2006; Eisenhardt et al. 2008; Jee et al. 2009; Huang et al. 2009; Rosati et al. 2009; Papovich et al. 2010; Schwope et al. 2010; Gobat et al. 2011; Jee et al. 2011; Foley et al. 2011) and the finding that some clusters at intermediate redshift ($z \sim 0.3$) have denser cores than clusters of similar mass produced in simulations (Broadhurst et al. 2008; Broadhurst & Barkana 2008; Oguri et al. 2009; Richard et al. 2010; Sereno et al. 2010; Zitrin et al. 2011a). While the evidence to date for early cluster growth is suggestive, possible explanations include departures from Gaussian initial density fluctuation spectrum or higher levels of dark energy in the past, so-called Early Dark Energy (EDE) (Fedeli & Bartelmann 2007; Sadeh & Rephaeli 2008; Francis et al. 2009; Grossi & Springel 2009). If a significant quantity of EDE (for example $\Omega_{DE} \sim 0.1$ at $z = 6$) suppressed structure growth in the early universe, then clusters would have had to start forming sooner to yield the numbers we observe today. These scenarios remain allowable within current observational constraints as described in the above papers, although some non-Gaussian models can be ruled out by using the cosmic X-ray background measurements (Lemze et al. 2009). The CLASH data permits significant advances to be made towards supporting or rejecting observational evidence for early cluster growth by measuring core densities for a larger, less biased sample of clusters.

In cosmological simulations, CDM-dominated halos of all masses consistently evolve to have a roughly "universal" density profile that steepens with radius. Functional forms that fit such a profile well include the "NFW" profile (Navarro et al. 1996, 1997) and the Einasto / Sérsic profile (Sérsic 1963; Einasto 1965; Navarro et al. 2004, 2010). Furthermore, each simulated halo's core density is related to the background density of the universe at the halo's formation time. Halos that form later, including the most massive galaxy clusters, are found to have the least dense cores in a relative sense. Determining the relationship between the shape and depth of a halo's gravitational potential and its total mass as a function of time thus provides fundamental constraints on structure formation.

In practice, the relative core densities, or "concentrations", are measured (both in simulated and observed halos) as $c_{vir} = r_{vir}/r_{-2}$, a ratio between the virial radius and the inner radius at which the density slope of the fitted profile is isothermal ($\rho \propto r^{-2}$). Analyses of gravitational lensing spanning such a large range of radius allows one to map the (primarily dark) matter profiles of observed halos and measure their concentrations.

Dark matter profiles are best mapped in cluster cores using strong lensing analysis of multiband *HST* imaging.

Table 1
Concentration Measurements for Previously Well-Studied Lensing-selected Clusters

Constraints[a]	Publication	Cluster	z	M_{vir} $[10^{15} M_\odot h^{-1}]$	c_{vir}	χ^2/d.o.f.
SL+WL+mag	Umetsu et al. (2011b)[b]	A1689	0.187	$1.34^{+0.20}_{-0.16}$	$13.82^{+1.72}_{-1.62}$	4.73/17
SL+WL+mag	Umetsu et al. (2011b)[b]	A1703	0.281	$1.29^{+0.22}_{-0.19}$	$6.89^{+1.04}_{-0.91}$	7.14/19
SL+WL+mag	Umetsu et al. (2011b)[b]	A370	0.375	$2.26^{+0.26}_{-0.23}$	4.56 ± 0.33	14.07/24
SL+WL+mag	Umetsu et al. (2011b)[b]	CL0024+17	0.395	$1.37^{+0.20}_{-0.18}$	$7.77^{+0.97}_{-0.87}$	11.47/20
SL+WL+mag	Umetsu et al. (2011b)[b]	RXJ1347.5-1145	0.451	$1.73^{+0.12}_{-0.11}$	$5.96^{+0.37}_{-0.35}$	45.06/25
RE+WL	Oguri et al. (2009)	SDSS J1531+3414	0.335	$0.7^{+0.29}_{-0.24}$	$7.9^{+3.0}_{-1.5}$	8.1/6
RE+WL	Oguri et al. (2009)	SDSS J1446+3032	0.464	$0.8^{+0.3}_{-0.22}$	$8.3^{+3.9}_{-3.1}$	6.4/6
RE+WL	Oguri et al. (2009)	SDSS J2111-0115	0.637	$0.9^{+0.41}_{-0.32}$	$14.1^{+25.9}_{-9.3}$	7.5/6

Note. — Of these 8 clusters, only one – RXJ1347.5-1145 – is in the CLASH sample.

[a] SL = strong lensing; WL = weak lensing; mag = magnification bias (number counts); RE = Einstein radius

[b] The parameters here are from standard NFW fits to profiles in Umetsu et al. (2011b), and not from the generalized NFW (gNFW) fits given in that paper.

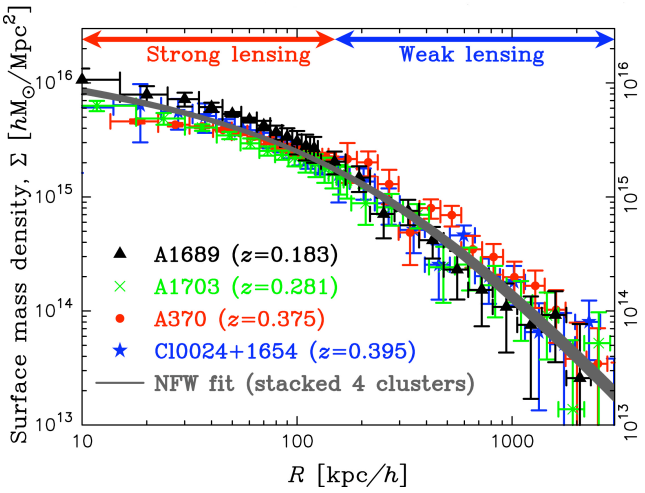

Figure 1. Mass profiles measured for four well-studied, strongly lensing galaxy clusters that are **not** included in the CLASH sample. All have similar mass profiles as measured from Hubble observations of strong-lensing and Subaru observations of weak-lensing distortion and magnification (Umetsu et al. 2011b, their Figure 6). The averaged mass profile is in remarkably good agreement with the standard NFW form (Umetsu et al. 2011a, their Figure 1) as shown by the gray area (2-σ confidence interval of the NFW fit), though with a higher concentration than predicted from cosmological simulations. Both strong and weak lensing probes are required to map the continuously steepening mass profile from the inner core (~ 10 kpc/h) out to beyond the virial radius (~ 2 Mpc/h).

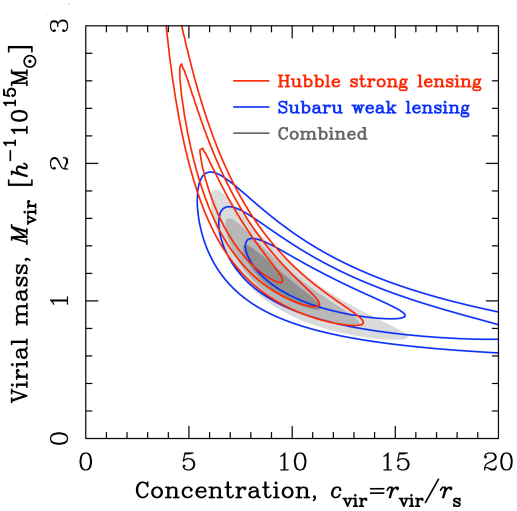

Figure 2. Joint strong and weak lensing analyses are required to obtain tight constraints on cluster concentrations as shown here for CL0024+17, a non-CLASH cluster (Umetsu et al. 2010, from their Figures 15 and 17). Confidence levels of 68.3%, 95.4%, and 99.7% are plotted in the $c_{\rm vir}$–$M_{\rm vir}$ plane.

The lensing-based mass profile mapping is extended to the virial radii of clusters using weak lensing analysis of wider field ground-based multiband imaging, such as from Subaru. Results from Umetsu et al. (2011b,a) for four of the currently best-studied (non-CLASH) clusters are shown in Figure 1.

Joint modeling of strong and weak lensing (SL+WL) yields significantly better constraints on concentrations than either probe alone. Quantitatively, Meneghetti et al. (2010a) found their joint SL+WL analyses of simulated clusters yield concentrations to $\sim 11\%$ accuracy, while WL-only and SL-only analyses yielded $\sim 33\%$ and $\sim 59\%$ scatters, respectively. Figure 2 demonstrates how SL and WL analyses combine to yield robust constraints on the mass and concentration of CL0024+17 (Umetsu et al. 2010).

The best studied (SL+WL) galaxy clusters to date have been found to have overly high concentrations (dense cores) compared to haloes in N-body simulations with similar masses, as shown in Figure 3 (Broadhurst et al. 2008; Oguri et al. 2009; Sereno et al. 2010) and detailed in Table 1. Recent simulations (Prada et al. 2011) yield cluster concentrations that are over 50% higher than previous simulations (e.g., Duffy et al. 2008). This is a product of upturns as a function of both mass and redshift found in these newer simulations, which are not yet understood. Similarly, clusters have also been found to have somewhat larger than expected Einstein radii, a direct and particularly accurate measure of the projected mass in a halo's core (Broadhurst & Barkana 2008; Richard et al. 2010; Zitrin et al. 2011a,b).

Unfortunately, the best studied clusters to date have also been among the strongest gravitational lenses known. Such lensing-selected clusters are highly biased toward halos with high concentrations, both intrinsically and as projected on the sky due to halo elongation along the line of sight (Hennawi et al. 2007; Oguri & Blandford 2009; Meneghetti et al. 2010b, 2011). These biases are estimated to lead to systematically higher concen-

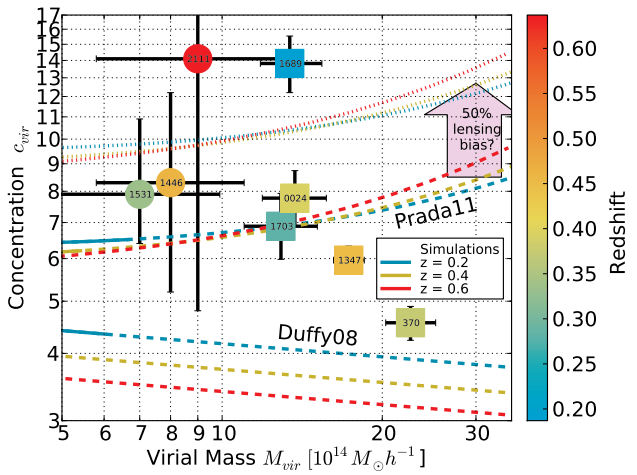

Figure 3. Mass profiles of the best studied clusters to date are revealed to have higher central density concentrations than simulated clusters of similar mass and redshift. Reconciliation may be within reach given results from the latest simulations and an estimated lensing bias which CLASH will avoid. The plotted lines are mean concentrations at three different redshifts for clusters in these simulations as calculated from the fitting formulae provided in those papers. However note that halos of this great mass are rare (or even non-existent at these redshifts) in these simulations, so these results are mainly extrapolations, as designated by the dashed lines. The thinner dashed lines above illustrate a 50% observational bias applied to the Prada et al. (2011) results. This bias has been roughly estimated for non-CLASH clusters such as these which were selected for study based on exceptional lensing strength (Hennawi et al. 2007; Oguri & Blandford 2009; Meneghetti et al. 2010a, 2011). Results from the currently best-studied clusters are plotted here as squares (Umetsu et al. 2011b) and circles (Oguri et al. 2009) labeled with abbreviated names and described further in Table 1.

trations by as much as 50% or more. However, such a bias is insufficient to account for the discrepancy between the observations and the predictions that is until a very recent analysis of new simulations was performed (see Figure 3 and discussion below).

More robust conclusions require analysis of a larger, unbiased cluster sample. Progress toward this goal has been made by LoCuSS, the Local Cluster Substructure Survey (Smith et al. 2005). A large sample of 165 clusters between $0.15 < z < 0.30$ was selected based on X-ray brightness. Strong lensing analyses of 20 of these based on *HST* imaging (mostly single-band "snapshots") were presented by Richard et al. (2010). Okabe et al. (2010a) published weak lensing analyses of 30 LoCuSS clusters, 22 of these being more "secure" based on multi-band Subaru imaging, and 9 of these 22 overlapping with the Richard et al. (2010) subset. Subaru images are especially desirable for WL studies as they enable excellent galaxy shape measurements to be performed over a wide area. Multiband imaging is also critical to properly select background galaxies and avoid significantly diluting the weak lensing signal (and thus the virial mass and concentration) with unlensed foreground galaxies (Medezinski et al. 2007, 2010). Stacked WL-only analyses have been performed on large cluster samples (Johnston et al. 2007; Mandelbaum et al. 2008), but we re-emphasize the need for combining strong + weak lensing analyses in addition to cross-comparisons with mass profile estimates from other techniques. For example, mass concentrations can be measured from X-ray profiles (Buote et al. 2007; Ettori et al. 2010), although these are subject to uncertainties due to assumptions about hydrostatic equilibrium. Importantly, cluster elongation along the line of sight (a potential bias in concentration measurements) can be measured by the combination of lensing and X-ray analysis (Morandi et al. 2010; Newman et al. 2011). The caustic technique (Diaferio & Geller 1997; Rines & Diaferio 2006) is, like lensing-based methods, independent of the dynamical state of the cluster and also provides an important cross check on mass estimates from lensing and gas kinematics. Further discussion of some of the previous results from various methods are given in Comerford & Natarajan (2007); Coe (2010); Rines et al. (2010); King & Mead (2011).

Reconciliation of high observed concentrations with results from simulations may ultimately come from significantly reducing the observational sample bias along with finding higher concentrations in simulated clusters. Baryons, for example, are currently absent from those cosmological simulations large enough to produce massive clusters. Baryons can result in significant "adiabatic contraction" on galaxy scales, however they constitute a much smaller fraction of the mass on cluster scales. Simulations including baryons show that cluster halo concentrations are likely only varied by $\sim 10\%$ or so relative to DM-only halos, and that the direction of variation (increase or decrease) is not even clear, depending on the gas physics assumed (Duffy et al. 2010; Mead et al. 2010; King & Mead 2011). Nonetheless, measuring the velocity dispersion of the Brightest Cluster Galaxy (BCG) as an additional constraint on the inner ($\lesssim 80$ kpc) mass profile, where its stellar mass is a non-negligible component of the matter distribution, provides for a more thorough mapping of the total mass profile. Some clusters have been shown to have inner mass profiles that are shallower than NFW (Sand et al. 2004, 2008; Newman et al. 2009, 2011). Deviations of cluster mass profiles from NFW or Einasto forms at small and/or large radii may slightly bias concentration measurements (Oguri & Hamana 2011). The use of multiple probes of the matter distribution, as CLASH is designed to do, will enable such biases to be measured and the significance of deviations determined.

More recently, an analysis by Prada et al. (2011) found that clusters in the Bolshoi and MultiDark simulations have concentrations $\sim 50\%$ higher than clusters in previous simulations. While the robustness of this new result is still being assessed, it raises the possibility that the combination of new observations of an unbiased sample of clusters and new simulations may be able to bridge the concentration gap. We stress here that estimates of the observational bias from previous cluster studies have large uncertainties and likely varies for each cluster. CLASH will determine mass profiles and concentrations for a new cluster sample free of lensing selection bias. As we demonstrate in §3.2, CLASH is designed to detect (or rule out) with 99% statistical confidence average deviations of 15% or more from predicted concentrations. However, given the outstanding uncertainties in the expected concentrations, we prefer to recast the problem as follows: CLASH will deliver robust observational concentration measurements for a sample of clusters that simulations will be tasked to reproduce. Ultimately this will lead to a better calibration of many mass estimation

techniques and, consequently, to a better understanding of structure formation on cluster scales and perhaps of our cosmological model as well.

2.2. *Improved Constraints on the Dark Energy Equation of State and SNe Evolution*

The biggest cosmological surprise in decades came from observations of high-redshift type-Ia supernovae (SNe Ia), providing the first evidence that the expansion of the Universe now appears to be accelerating (Riess et al. 1998; Perlmutter et al. 1999), and indicating the Universe is dominated by "dark energy." The presence of dark energy has galvanized cosmologists as they seek to understand it. Observations of high-redshift SNe Ia have continued to lead the way in measuring the properties of dark energy (e.g., Riess et al. 2011). The goal for cosmologists now is to measure the equation of state of dark energy, $w = P/(\rho c^2)$, and its time variation in the hope of discriminating between viable explanations. A departure of the present equation of state, w_0, from -1 or a detection of its variation, $\partial w/\partial z$, would invalidate an innate vacuum energy (i.e., the cosmological constant) as the source of dark energy and would point towards a present epoch of "weak inflation." A difference between the expansion history and the growth history of structure expected for $w(z)$ would point towards a breakdown in General Relativity as the cosmic scale factor approaches unity.

HST paired with *ACS* is a unique tool in this investigation, providing the only means to collect SNe Ia at $1 < z < 1.5$, which, in turn, provide the only constraints we have to date on the time variation of w. From the 23 SNe Ia at $z > 1$ with *HST* data (Riess et al. 2004, 2007) we have learned: 1) that cosmic expansion was once decelerating before it recently began accelerating, 2) that dark energy, i.e., an energy density with $w < 0$, was already present during this prior decelerating phase, 3) that SNe Ia at a look-back time of 10 Gyr appear both spectroscopically and photometrically similar to those seen locally and 4) no rapid change is seen in $w(z)$ and thus no departure is yet seen from the cosmological constant, though the constraint on the time variation remains an order of magnitude worse than on the w_0.

SNe Ia play a central role not only as distance indicators for cosmography, but also as major contributors to cosmic metal production and distribution. The measurement of high-redshift SN Ia rates is therefore integral to understanding the history of chemical enrichment. The high-redshift rate cannot easily be predicted from the star formation rate because the nature and, hence, the timescales of the process behind the growth of the white dwarf toward the Chandrasekhar mass is not known. The two leading competing scenarios are accretion from a close binary companion – the single-degenerate scenario (Whelan & Iben 1973; Nomoto 1982) or merger with another white dwarf, following loss of orbital energy and angular momentum by emission of gravitational waves – the double-degenerate scenario (Iben & Tutukov 1984; Webbink 1984). One way to constrain the different progenitor scenarios is to measure the delay-time distribution (DTD) of SNe Ia. This is the distribution of times that elapse between a brief burst of star formation, and the subsequent SN Ia explosions. Observations have suggested various different forms for the DTD (e.g., (Dahlen et al. 2004, 2008; Mannucci et al. 2006; Pritchet et al. 2008)). However, a number of more recent measurements and analyses point to a DTD that is a power law of index ≈ -1 (Totani et al. 2008; Maoz et al. 2010; Maoz & Badenes 2010; Brandt et al. 2010; Horiuchi & Beacom 2010; Maoz et al. 2011; Graur et al. 2011). Specifically, Graur et al. (2011) have shown that such a DTD fits well the measured SN Ia rate out to $z \approx 2$. Small sample sizes are the major limiting factor at high redshifts. Large high-z SN samples are therefore needed to resolve the issue, and control possible biases in cosmological studies (due to the evolving SN Ia channel mix).

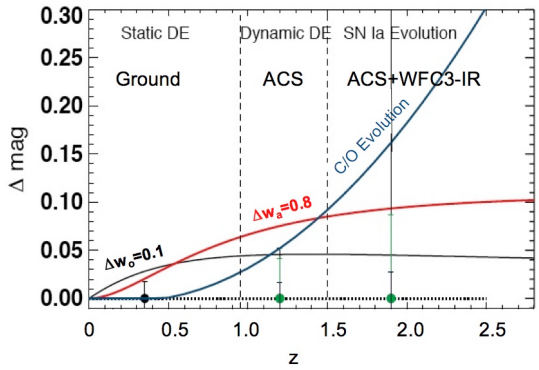

Figure 4. Dark Energy and Evolution Sensitivity. Three models consistent with current data are shown: $w_0 = 0.9$, $w_a = 0$ (black); $w_0 = 1$, $w_a = 0.8$ (red); and $w_0 = 1$, $w_a = 0$ (dashed). Also plotted blue is the SNe Ia evolution model of Domínguez et al. (2001), where the peak luminosity changes 3% per solar mass change in the donor star. The error bars show the constraints at present, as projected after CLASH, and if *HST* continues to collect SNe Ia at the present rate for 7 years.

The CLASH survey uses *ACS* in parallel with the cluster program to continue the discovery of SNe Ia at $1 < z < 1.5$, the objects which tell us about the variation in w. With *WFC3* in parallel, CLASH will yield SNe Ia at $1.5 < z < 2.5$ (Rodney et al. 2011). Observations in this fully matter dominated epoch provide the unique chance to test SN Ia distance measurements for the deleterious effects of evolution independent of our ignorance of dark energy (Riess & Livio 2006). Because the SNe Ia are detected when these cameras are in parallel, they are far from the cluster core (~ 2 Mpc at the median cluster redshift of $z = 0.4$) and, hence, the effects of lensing are small (and correctable), making the SNe usable for improving the limits on the redshift variation of the dark energy equation of state. At $z < 1$, SN Ia distance measurements are most sensitive to the static component of dark energy, w_0. At $1 < z < 1.5$, the measurements are most sensitive to the dynamic component, w_a. By $z > 1.5$, the measurements are most sensitive to evolution if present (e.g., the changing C/O ratio of the donor star), providing the means to diagnose and calibrate the degree of SN Ia evolution in dark energy measurements. Figure 4 shows how variations in the DE equation of state or an evolution in the white dwarf C/O ratio can change the SN Ia distance modulus as a function of redshift.

Accounting for the systematic uncertainty introduced by the cosmic star formation history, Graur et al. (2011) predicted the SN Ia rate out to higher redshifts (their figure 13), which we use here, in conjunction with the CLASH observational parameters, to estimate the num-

Table 2
Estimated Number of $z \geq 1$ SNe Ia to be Discovered During the CLASH Program

Redshift Range	Estimated Number of SNe Ia Found
$1.0 \leq z < 1.5$	7 – 11
$1.5 \leq z < 2.0$	4 – 13
$2.0 \leq z \leq 2.7$	0 – 4
$1.0 \leq z \leq 2.7$	11 – 28

Note. — These estimates are the 68% confidence intervals, accounting for both statistical and systematic uncertainties. The assumed SN Ia rate is from Graur et al. (2011).

ber of $z \geq 1$ SNe Ia that will be discovered over the course of this program. These estimates are presented in Table 2 and are the 68% confidence intervals, accounting for both statistical and systematic uncertainties.

2.3. *Detection and Characterization of $z > 7$ Galaxies*

One of the most important goals in observational cosmology is to find the first generation of galaxies and understand their roles in the reionization of the intergalactic medium (IGM) between $z \sim 6$ to $z \sim 12$. Substantial progress has been made in recent years in finding objects at $z \sim 6 - 7$ (Bouwens et al. 2006, 2009; Bunker et al. 2010; Oesch et al. 2010a,b; McLure et al. 2010; Capak et al. 2011), which are, at most, $\sim 700 - 900$ Myr of age. We wish to find objects at even earlier epochs, in order to understand (1) how the first galaxies were formed through a hierarchical merging process; (2) how the chemical elements were generated and redistributed through the galaxies; (3) how the central black holes exerted influence over the galaxy formation; and (4) how these objects contributed to the end of the "dark ages."

The majority of galaxies at $z = 6 - 7$ have been discovered via two methods: (1) deep pencil-beam surveys, such as the Hubble Ultra Deep Field (HUDF; Beckwith et al. (2006)) and the Great Observatories Origins Deep Survey (GOODS; Giavalisco et al. (2004)); and (2) degree-size surveys with 10m-class ground-based telescopes, such as the Subaru Deep Field. Both use a color selection to search for "dropout" candidates – galaxies with deep IGM absorption at the wavelengths shortward of the redshifted Lyα break. These efforts have proven successful at finding objects at $z < 7$, but there is growing evidence for a rapid decrease in the number of candidates at higher redshifts (Iye et al. 2006; Bouwens et al. 2006; Castellano et al. 2010). *HST/WFC3* data yields 73 $z \sim 7$ and 59 $z \sim 8$ candidates (Bouwens et al. 2010). These results are based on ~ 500 orbits of HUDF observations. In comparison, > 600 galaxies are found at $z \sim 6$ (Bouwens et al. 2007; Su et al. 2011). To date, there have been only two or three spectroscopically confirmed galaxies at $z > 7$ (Lehnert et al. 2010; Ono et al. 2012; Schenker et al. 2012) and one spectrum for a Gamma Ray Burst at $z \sim 8.2$ (Salvaterra et al. 2009; Tanvir et al. 2009). The reason, in part, is a lack of photons: at redshift $z = 8$ and 10, an L^* galaxy would have an apparent magnitude in the first NIR detection band of 28.2 and 29.6, respectively.

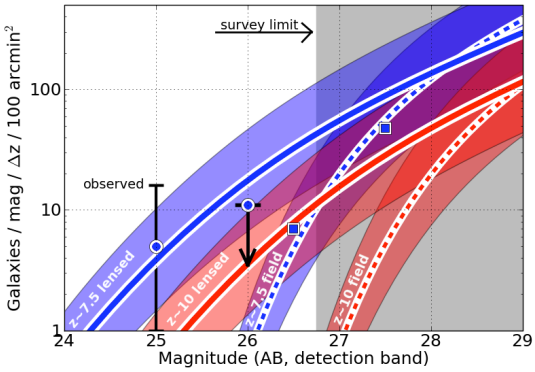

Figure 5. The estimated number counts in the total CLASH survey at $z \sim 7.5$ and 10 are plotted as the solid "lensed" blue and red lines, respectively, as functions of magnitudes in the detection bands F110W and F160W. Note the large uncertainties (shaded regions). A NIR survey of a comparable area (100 square arcmin) in unlensed fields would have a $\sim 10\times$ lower efficiency at these magnitudes (in agreement with Maizy et al. 2010). We have assumed an evolving Schechter luminosity function with $dM^\star/dz = 0.36$ as derived by (Bouwens et al. 2006, 2008) and plotted as the dashed lines with shaded uncertainties. Observed number counts from Bouwens et al. (2009) are plotted as squares. Lensing estimates were derived using the Zitrin et al. (2009) CL0024+17 mass model to simulate the magnifications of sources and reduction of source area. These estimates are in agreement with observed lensed counts in cluster fields plotted as circles (Bouwens et al. 2009).

Gravitational lensing by clusters amplifies the flux of background sources considerably. These cosmic telescopes improve the efficiency of searches for relatively bright high redshift galaxies (Bouwens et al. 2009; Maizy et al. 2010). In fact, the majority of $m < 25.5$ AB, $z \gtrsim 6.5$ galaxy candidates have been found in cluster fields (e.g., Kneib et al. 2004; Bradley et al. 2008; Zheng et al. 2009; Bradley et al. 2011; Schenker et al. 2012). Interestingly, most of these candidates are found in regions with amplification of ~ 10. Furthermore, lens models can be used to help discriminate between highly-reddened objects and truly distant, high redshift objects, as the projected positions of the lensed images are strong functions of the source redshifts.

Luminous $z > 7$ galaxies are extremely valuable as their spectra can be used to determine the epoch of the IGM reionization. This is because only a tiny fraction of neutral hydrogen is needed to produce the high opacity of Lyα observed at $z \sim 6$. The damped Lyα absorption profile that results from a completely neutral IGM (Miralda-Escude 1998) can be measured even at low-spectral resolution. Furthermore, direct measurements of the early star-formation rate (via Lyα and Hα emission, Iye et al. 2006) can be derived from the spectra of bright high-z galaxies. CLASH may detect dozens of relatively bright (magnified to $m < 26.7$ AB) $z > 7$ galaxies, including some bright enough for spectroscopic follow-up. A NIR survey of a comparable area (100 square arcmin) in unlensed fields would have a $\sim 10\times$ lower efficiency. An estimate, albeit a highly uncertain one, of the CLASH high-z detection efficiency enhancement is shown in Figure 5.

2.4. *Galaxy Evolution*

ΛCDM provides a robust theoretical framework for the evolution of dark matter haloes. However, the formation of galaxies within these haloes is governed by com-

plicated baryonic interactions that are difficult to simulate on cosmological scales. The gap in our understanding of the connection between the formation of galaxies and that of their parent haloes is illustrated by observations of galaxy "downsizing" (Cowie et al. 1996). ΛCDM predicts that structures form hierarchically, with small haloes forming early and later assembling into larger haloes. In contrast, massive galaxies appear to have formed at early times, as evidenced by the redshift at which their star formation peaks (e.g., Cowie et al. 1996; Guzman et al. 1997; Brinchmann & Ellis 2000; Juneau et al. 2005) and the old ages of their stellar populations at $z = 0$ (e.g., Faber et al. 1995; Worthey 1996; Proctor & Sansom 2002; Thomas et al. 2005). The stellar mass density of the universe is also increasing with cosmic time, as galaxies form stars, then shut down their star formation and, ultimately, accumulate on the red sequence(Bell et al. 2004; Faber et al. 2007).

Several open questions remain about the origin and nature of this stellar mass growth. Is it dominated by *in situ* star formation, or through mergers of existing stellar systems? How does the balance of these two processes change with galaxy mass and cosmic time? In a system dominated by hierarchical assembly, this is akin to asking whether most of the mass accreted by galaxies comes in as gas (e.g., the "cold flows" of Kereš et al. 2005; Dekel & Birnboim 2006) or as stars (e.g., "dry mergers", Khochfar & Burkert 2003; Bell et al. 2004). Theoretical expectations predict that the *in situ* population should be very centrally concentrated, while an accreted stellar component should extend to larger radius (Oser et al. 2010). Thus massive galaxies are predicted to have substantial gradients in the origin of their stars, with the innermost stars having formed *in situ* and the outer stars largely accreted through merging.

Recent work has demonstrated that massive, passive galaxies already exist at $z \sim 2$ (e.g., Trujillo et al. 2006; Kriek et al. 2009) and that these systems are much more compact than local massive galaxies (Trujillo et al. 2006; Longhetti et al. 2007; van Dokkum 2008), suggesting that they must grow significantly in size between $z \sim 2$ and $z \sim 0$. This process likely happens through "dry" (dissipationless) merging, since such massive galaxies are observed to have old stellar populations locally. There are also substantial populations of massive star-forming galaxies over a similar redshift range. These galaxies tend to exhibit large star forming "clumps" (Cowie et al. 1995; van den Bergh 1996; Elmegreen et al. 2004a,b), although at least some of these galaxies may form disks with coherent rotation (Genzel et al. 2010).

There are several observational challenges to measuring and characterizing these two modes of growth. It is difficult to resolve substructure in high-redshift galaxies, even from space. Both resolution and signal-to-noise considerations limit observations to the upper end of the mass function. Searches that use a small number of imaging filters struggle to identify the redshifts (and therefore the masses) of the targets and can only poorly constrain their spectral energy distributions (SEDs) and stellar populations. Studies that rely on emission lines probe only the assembly of star-forming galaxies.

The CLASH program is well suited for studying galaxy assembly at $z < 3$. The high magnification and spatial stretching of strongly lensed distant galaxies, coupled with the broad 16-band photometry and resulting photometric redshifts, enables the measurement of star formation rates and stellar ages in each lensed galaxy over many resolution elements. The magnification makes it possible to resolve substructures in high-redshift lensed galaxies further down the galaxy mass function than is possible in unlensed galaxies at similar redshifts. In addition, with CLASH, we can contrast the relative properties of galaxy cores versus their outer regions, and (where they exist) the properties of substructures such as clumps, spiral arms, and ongoing mergers. In the full CLASH sample of 25 clusters, we expect to find several strongly lensed background galaxies per cluster that are suitable for such analyses, providing a sample of 50 to 100 galaxies with $1 < z < 3$.

3. CLASH CLUSTER SAMPLE

The CLASH program is robustly measuring galaxy cluster dark matter profiles and concentrations for a systematic comparison with those realized in cosmological simulations. Specifically, our cluster sample size and selection criteria were chosen to allow the robust measurement of deviations from the predicted cluster concentration distribution of $\sim 15\%$ or more at high statistical confidence ($\sim 99\%$ C.L.) given a relatively unbiased ensemble of clusters (§2.1).

3.1. *Cluster Sample Selection*

To date, robust joint SL+WL analyses have only been performed on a small, highly-biased sample of five to ten clusters (Table 1 and Figure 3). These clusters were selected for study primarily based on their gravitational lensing strength, which tends to preferentially select systems with higher central matter concentrations. To establish a sample that is largely free of lensing bias, we selected 20 massive clusters from X-ray-based compilations of dynamically relaxed systems. Sixteen of these 20 clusters were taken from the Allen et al. (2008) compilation of massive relaxed clusters. Clusters in our X-ray selected subsample all have $T_x \geq 5$ keV and exhibit a high degree of dynamical relaxation as evidenced by *Chandra X-ray Observatory* images that show well-defined central surface brightness peaks and nearly concentric isophotes. The clusters, in general, also show minimal evidence for departures from hydrostatic equilibrium in X-ray pressure maps. Most of the 20 clusters have smooth and only mildly elliptical ($\langle\epsilon\rangle = 0.19$) X-ray emission and a BCG within a projected distance of 23 kpc of the X-ray centroid. No lensing information was used a priori to select them in order to ensure that they are not preferentially aligned along the line of sight, in contrast with a purely lensing-selected sample, where the surface mass density is, on average, biased upwards along the line of sight by intrinsic triaxiality (Hennawi et al. 2007; Oguri et al. 2009; Meneghetti et al. 2010a, 2011). A handful of the clusters in the CLASH X-ray selected subset have some evidence for departures from symmetric X-ray surface brightness distributions. These systems are briefly discussed in §3.3.

These 20 clusters comprise the primary sample for our DM distribution studies. Existing X-ray data will be used to measure the gas density profile for subtraction from the total mass profile (as applied by Lemze et al.

(2008) for A1689), which is necessary when making detailed comparison with the predictions of DM-only simulations. Although these clusters are X-ray selected, one or more lensed arcs are indeed visible in all of the clusters for which sufficiently high-quality imaging was available. This indicates the X-ray selected clusters in our sample have Einstein radii in the range $15''$ to $35''$. X-ray images from the ACCEPT[25] database for these 20 CLASH clusters are shown in Figure 6.

In addition, CLASH includes five clusters selected based solely on their exceptional strength as gravitational lenses (large Einstein radii, $\theta_{Ein} > 35''$ for $z_s = 2$). Analysis of these clusters will allow us to further quantify the lensing selection bias toward high concentrations. The excellent strong lensing data yielded by these clusters will enable derivation of some of the highest resolution dark matter maps which may be obtained (as in Coe et al. 2010). The primary motivation for selecting these five "high-magnification" clusters, however, was to significantly increase the likelihood of discovering very highly magnified high redshift galaxies (§2.3). While most of the CLASH clusters lie behind regions of low Galactic extinction (median E(B-V) = 0.026), there is one cluster, MACS2129.4-0741, with significant amounts of Galactic cirrus located northeast of the cluster core. Because this cluster has one of the larger Einstein radii known, its inclusion in the "high-magnification" sample was deemed worthwhile in spite of the presence of this cirrus.

Figure 7 shows, respectively, the distribution of the projected separation between the BCG and the peak of the X-ray surface brightness and the distribution of the ellipticity of the X-ray emission for the CLASH sample. Ellipticity measurements are from Maughan et al. (2008). The X-ray selected cluster sub-sample exhibits, on average, a very small offset between the BCG and peak X-ray flux. The X-ray selected cluster sub-sample also exhibits a lower average ellipticity than our high-magnification (Einstein-radii selected) sample but is consistent with the mean ellipticity of the larger Maughan et al. (2008) sample.

The 25 clusters in the CLASH program are presented in Table 3 and some of their key X-ray properties are given in Table 4, including the bolometric luminosity (defined for convenience to be between 0.1 and 100 keV), temperature, and cluster-to-solar [Fe/H] ratio, where the solar abundance reference is from Anders & Grevesse (1989). Table 4 also lists the source of the X-ray selection in column 6. The CLASH sample is drawn heavily from the Abell and MACS cluster catalogs (Abell 1958; Abell et al. 1989; Ebeling et al. 2001, 2007, 2010). The CLASH clusters span almost an order of magnitude in mass (~ 5 to $\sim 30 \times 10^{14}$ $M_\odot$). These clusters were also selected to cover a wide redshift range ($0.18 < z < 0.90$ with a median $z_{med} = 0.40$) allowing us to probe the full $c(M, z)$ relations expected from simulations.

The X-ray parameters in Table 4 are derived by us using `CIAO v4.3` and `CALDB v4.4.3`. We filtered the Chandra data for flares and reprojected the deep Chandra background fields to match the cluster observations. The background data were also filtered for "status= 0" events to be suitable for use with the `VFAINT` mode data. To obtain X-ray luminosities and temperatures uniformly across the sample, we extracted spectra from apertures with radii of 714 kpc (500 h_{100}^{-1} kpc) and excluded the central 71.4 kpc (50 h_{100}^{-1} kpc). These "core-excised" spectra provide X-ray temperature estimates that are relatively unaffected by the presence or absence of a cool core (e.g., Markevitch (1998)). Figure 8 shows the X-ray temperature, T_x, as a function of the scaled bolometric luminosity, $L_x/E(z)$, for CLASH clusters using the data in Table 4. The X-ray luminosities are scaled assuming self-similar evolution, $E(z) = \sqrt{\Omega_m(1+z)^3 + \Lambda}$, to allow direct comparison to the low-redshift luminosity temperature relationships from Markevitch (1998) and Pratt et al. (2009) (L_2 (measured within 0.15-1.00 R_{500}) vs. T_3 (0.15-0.75 R_{500}), to be specific.) We verified that the deep background particle event rates matched that seen in the cluster spectra between $9 - 12$ keV. The X-ray counts were binned to a minimum of 20 counts per energy bin. Since the extracted spectra were dominated by source counts, the results were not very sensitive to the background scaling. To estimate the cluster temperature, we used `XSPEC 12.6.0q` to fit the X-ray spectra between $0.7 - 7.0$ keV. We assumed a single temperature plasma model (the `XSPEC` apec model) absorbed by a Galactic hydrogen column fixed to the value obtained from the Bell survey (Dickey & Lockman 1990). The metallcity, temperature, and normalization were allowed to be free. The best fit temperatures and 1σ error bars, and the bolometric X-ray luminosities are reported in Table 4.

3.2. *Cluster Sample Size Requirements*

The required size of our "relaxed" cluster sample is derived from the goal to measure "average" cluster concentrations to $\sim 10\%$ (after accounting for variations in mass and redshift) and to detect a $\sim 15\%$ deviation from the concentrations of simulated clusters at 99% confidence.

Statistically, if we assume measurement errors are independent and normally distributed then the number of clusters, N_{clus}, needed to measure the average concentration to a fractional accuracy of f is just

$$N_{clus} = (\sigma_{tot}/f)^2 \quad (1)$$

where the total scatter in an individual measurement of the concentration, σ_{tot}, is

$$\sigma_{tot}^2 = \sigma_{int}^2 + \sigma_{LSS}^2 + \sigma_{meas}^2 \quad (2)$$

and includes contributions from intrinsic variation (including the effects of orientation averaging of triaxial halo shapes), variations due to intervening large scale structure (LSS), and measurement uncertainties. Concentrations of relaxed simulated cluster halos have intrinsic scatters of $\sim 30\%$ (e.g., Neto et al. 2007; Macciò et al. 2008; Duffy et al. 2008). LSS can scatter concentration measurements by $\sim 13\%$ (Hoekstra et al. 2002). And we conservatively estimate measurement uncertainties to be $\sim 37\%$ as follows based on empirical data (though analysis of simulated data suggests $\sim 11\%$ accuracy is possible Meneghetti et al. 2010a).

Analysis of CL0024+17 yielded a concentration measurement uncertainty of $\sim 22\%$ (Umetsu et al. 2010), which we will use here as a baseline. We assume here

[25] ACCEPT = Archive of Chandra Cluster Entropy Profile Tables. See http://www.pa.msu.edu/astro/MC2/accept/ for more information

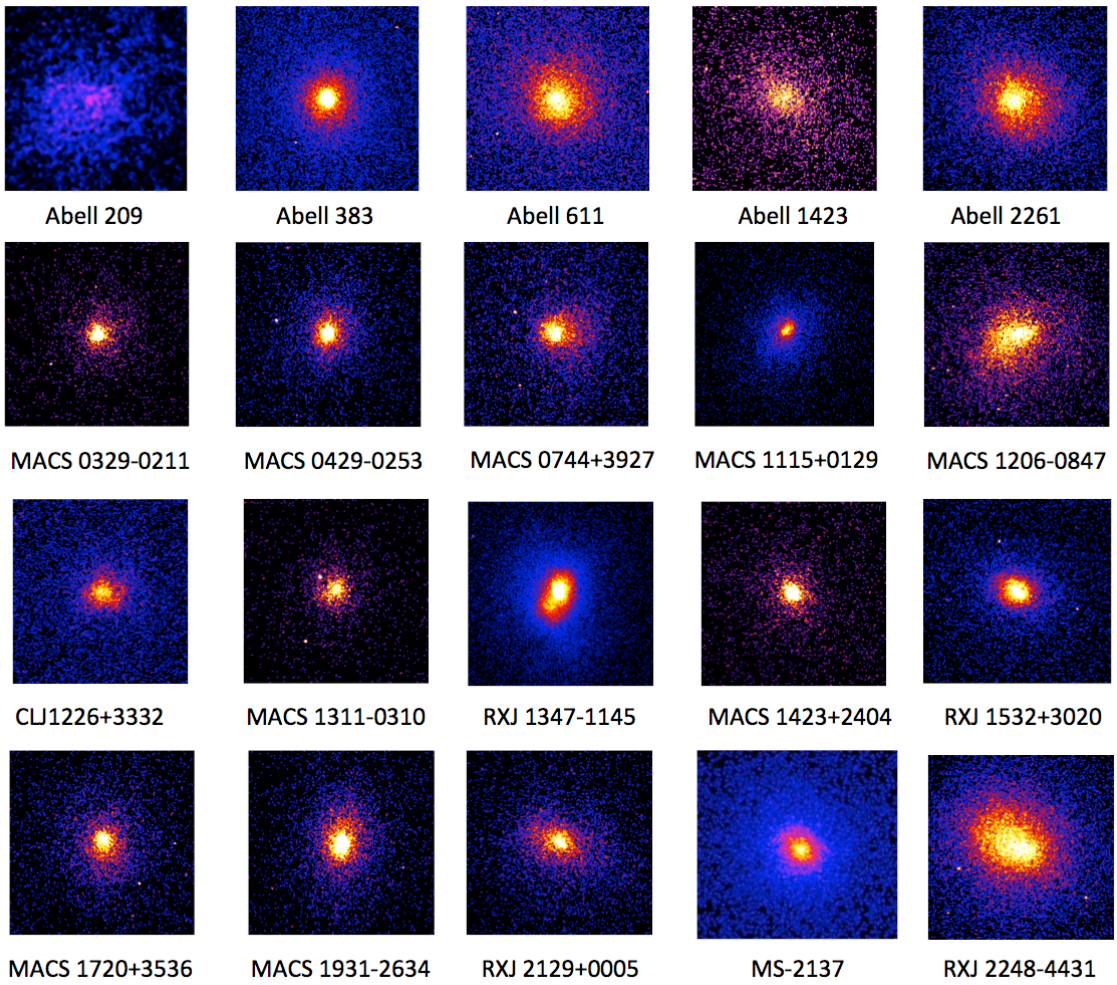

Figure 6. Cutouts of Chandra X-ray images centered on the 20 CLASH clusters in the X-ray selected subsample. These images are taken from the Archive of Chandra Cluster Entropy Profile Tables (ACCEPT). Each cutout subtends ∼3.45 arcminutes, which is nearly the same as the *ACS/WFC* field of view on *HST*.

that our precisions will be dominated by the quality of our SL data and that our measurement uncertainty will scale roughly as $\sigma \propto 1/\sqrt{N_{arc}} \propto 1/R_E$, where for CL0024+17 with $R_E \sim 35''$, $N_{arc} = 33$ arcs were detected. Note we have also assumed $N_{arc} \propto R_E^2$. Based on archival *WFPC2* and *ACS* images, we measured a mean $R_E \approx 20''$ for our sample of 20 relaxed clusters, which should conservatively yield $N_{arc} \sim 12$ arcs per cluster. This scales the $\sim 22\%$ uncertainty for CL0024+17 with 33 arcs up to a conservative $\sim 37\%$ for an average cluster with just 12 arcs.

Adopting $\sigma_{int} = 0.30$, $\sigma_{LSS} = 0.13$ and $\sigma_{meas} = 0.37$, we find $\sigma_{tot} = 0.49$, and hence, if $f = 0.10$ then $N_{clus} \sim 24$. This empirical sample size estimate is consistent with one derived from numerical simulations of strong lensing, as shown in Figure 9. The approximately log-normal distribution of DM halo concentrations seen in such simulations (Meneghetti et al. 2010b) indicates that ∼20 massive clusters ($M_{vir} > 5 \times 10^{14}$ $M_\odot$) are required to detect 15% deviations from expectations in the standard cosmological model at 99% confidence.

Note that we may expect deviations to be greater than 15% if results from lensing-selected clusters are any indication. Simulated $10^{15} M_\odot h^{-1}$ clusters at $z = 0$ typically have $c_{vir} \sim 5$ (e.g., Duffy et al. 2008). For this fiducial cluster, Oguri et al. (2009) instead find $c_{vir} \sim 12$ for observed clusters (based on a fit to values observed for 10 lensing clusters accounting for the various masses and redshifts). Even after including a 50% lensing bias, these observed concentrations are still $\sim 70\%$ greater than expectations. Being more conservative and assuming a factor of 2 (100%) lensing bias (Meneghetti et al. 2010a), the observed concentrations would still be $\sim 20\%$ greater than expectations. Although as discussed in §2.1, more recent simulations (Prada et al. 2011) may alleviate these discrepancies.

3.3. *Notes on Clusters with Possible Substructure*

While our X-ray selection criteria favors the inclusion of highly relaxed clusters in the CLASH sample, for 8 of our clusters the dynamical state is somewhat ambiguous. Some researchers have reported evidence for substructure in the X-ray surface brightness profiles of these 8 clusters. The presence of substructure may suggest that a cluster is not fully dynamically relaxed. We summarize this evidence below. We note that the presence of a minor degree of substructure does not inhibit our ability to determine a cluster's mass profile characteristics. In simulations,

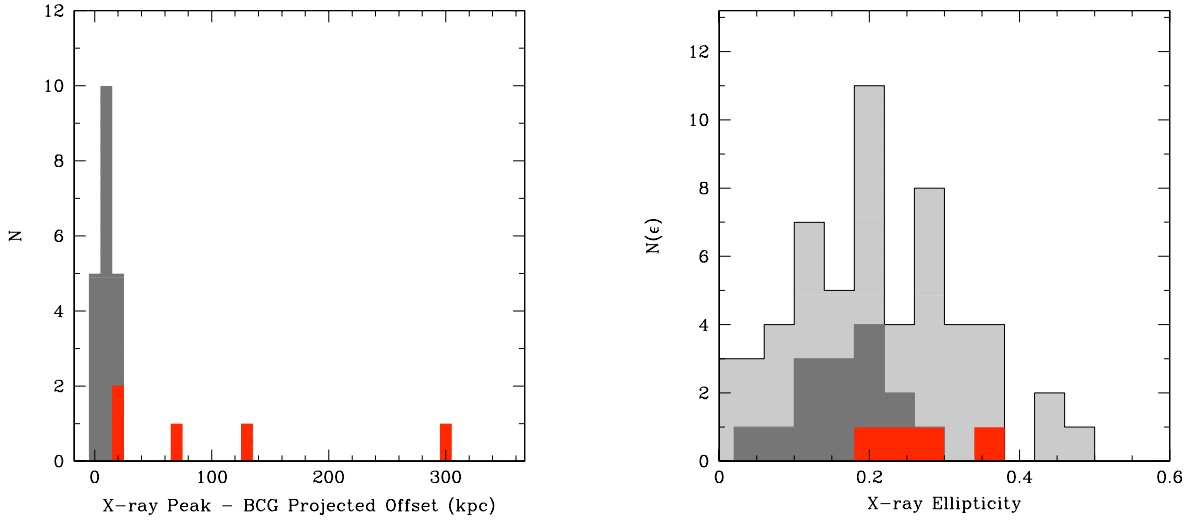

Figure 7. **Left:** The distribution of the projected separation between the Brightest Cluster Galaxy (BCG) and the peak of the X-ray surface brightness for the X-ray selected (dark grey) and Einstein-radii selected (red) cluster subsamples. The average projected BCG - X-ray peak separation for the X-ray selected sample is 10.4 kpc. **Right:** The distribution of the ellipticity of the X-ray emitting intracluster gas for the X-ray selected (dark grey) and Einstein-radii selected (red) cluster subsamples. The distribution of the ellipticities of the 96 clusters in the Maughan et al. (2008) sample that are **not** in common with CLASH is shown in the light grey histogram. The mean X-ray emission ellipticities for the X-ray and Einstein-radii selected cluster samples are 0.19 and 0.28, respectively.

Table 3
The CLASH Cluster Sample and *HST* Observing Plan

Cluster	α_{J2000}	δ_{J2000}	z_{Clus}	HST Cycle	CLASH Orbits	Program ID	Archival Orbits[c]
X-ray Selected Clusters:							
Abell 209	01:31:52.57	−13:36:38.8	0.206	19	20	12451	(3)
Abell 383	02:48:03.36	−03:31:44.7	0.187	18	20	12065	(3)
MACS0329.7-0211	03:29:41.68	−02:11:47.7	0.450	19	20	12452	(2.5)
MACS0429.6-0253	04:29:36.10	−02:53:08.0	0.399	20	20	12788	(0.5)
MACS0744.9+3927	07:44:52.80	+39:27:24.4	0.686	18	17	12067	6
Abell 611	08:00:56.83	+36:03:24.1	0.288	19	18	12460	2
MACS1115.9+0129	11:15:52.05	+01:29:56.6	0.352	19	20	12453	0.5
Abell 1423	11:57:17.26	+33:36:37.4	0.213	20	20	12787	(0.5)
MACS1206.2-0847	12:06:12.28	−08:48:02.4	0.440	18	20	12069	0.5 + (0.5)
CLJ1226.9+3332	12:26:58.37	+33:32:47.4	0.890	20	18	12791	16
MACS1311.0-0310	13:11:01.67	−03:10:39.5	0.494	20	20	12789	0
RXJ1347.5-1145	13:47:30.59	−11:45:10.1	0.451	18	15	12104	6 + (0.5)
MACS1423.8+2404	14:23:47.76	+24:04:40.5	0.545	20	17	12790	5
RXJ1532.9+3021	15:32:53.78	+30:20:58.7	0.345	19	20	12454	(0.5)
MACS1720.3+3536	17:20:16.95	+35:36:23.6	0.391	19	20	12455	(0.5)
Abell 2261	17:22:27.25	+32:07:58.6	0.224	18	20	12066	(0.5)
MACS1931.8-2635	19:31:49.66	−26:34:34.0	0.352	19	20	12456	0
RXJ2129.7+0005	21:29:39.94	+00:05:18.8	0.234	19	20	12457	(1)
MS2137-2353	21:40:15.18	−23:39:40.7	0.313	18	18	12102	5 + (7)
RXJ2248.7-4431 (Abell 1063S)	22:48:44.29	−44:31:48.4	0.348	19	20	12458	(0.5)
High Magnification Clusters:							
MACS0416.1-2403	04:16:09.39	−24:04:03.9	0.42[b]	19	20	12459	(1)
MACS0647.8+7015	06:47:50.03	+70:14:49.7	0.584	18	18	12101	9
MACS0717.5+3745	07:17:31.65	+37:45:18.5	0.548	18	17	12103	7
MACS1149.6+2223	11:49:35.86	+22:23:55.0	0.544	18	18	12068	5
MACS2129.4-0741	21:29:26.06[a]	−07:41:28.8[a]	0.570	18	18	12100	5

[a] Central cluster coordinates derived from optical image instead of X-ray image
[b] Cluster redshift for MACS0416.1−2403 is based on *Chandra* X-ray spectrum (this work). Uncertainty on this value is ±0.02. For this fit, the core was not excluded. To maximize the counts, an aperture of 714 kpc was used, binned to achieve a minimum of 20 counts per energy bin. The background in the 0.7-7.0 keV range was fit from the *Chandra* deep fields.
[c] Archival *ACS* or *WFPC2* imaging data only; *WFPC2* orbits shown in parentheses. Archival *ACS* images, when available, are used in conjunction with new CLASH data to achieve the desired depths in all filters.

Table 4
X-ray Properties of the CLASH Cluster Sample

Cluster	kT (keV)	$(L_{Bol})^a$ (10^{44} erg s^{-1})	[Fe/H] Ratio (Cluster/Solar)^c	Ellipticity^b ϵ	Centroid Shift^b $\langle w\rangle(10^{-2}R_{500})$	X-ray Morphology Reference
X-ray Selected Clusters:						
Abell 209	7.3 ± 0.54	12.7 ± 0.3	0.18 ± 0.09	0.21 ± 0.01	0.55 ± 0.05	1
Abell 383	6.5 ± 0.24	6.7 ± 0.2	0.59 ± 0.10	0.04 ± 0.01	0.18 ± 0.02	2
MACS0329.7-0211	8.0 ± 0.50	17.0 ± 0.6	0.48 ± 0.10	0.15 ± 0.03	1.38 ± 0.13	2,3
MACS0429.6-0253	6.0 ± 0.44	11.2 ± 0.5	0.34 ± 0.11	0.21 ± 0.02	0.38 ± 0.03	2,3
MACS0744.9+3927	8.9 ± 0.80	29.1 ± 1.2	0.37 ± 0.10	0.11 ± 0.02	1.41 ± 0.13	2,3
Abell 611	7.9 ± 0.35	11.7 ± 0.2	0.30 ± 0.07	···	···	2
MACS1115.9+0129	8.0 ± 0.40	21.1 ± 0.4	0.32 ± 0.06	···	···	2,3
Abell 1423	7.1 ± 0.65	7.8 ± 0.2	0.23 ± 0.13	···	···	4
MACS1206.2-0847	10.8 ± 0.60	43.0 ± 1.0	0.25 ± 0.09	···	···	3,4
CLJ1226.9+3332	13.8 ± 2.80	34.4 ± 3.0	0.36 ± 0.25	0.10 ± 0.03	1.30 ± 0.11	2
MACS1311.0-0310	5.9 ± 0.40	9.4 ± 0.4	0.42 ± 0.10	0.08 ± 0.02	0.39 ± 0.03	2,3
RXJ1347.5-1145	15.5 ± 0.60	90.8 ± 1.0	0.20 ± 0.06	0.26 ± 0.01	0.63 ± 0.05	2
MACS1423.8+2404	6.5 ± 0.24	14.5 ± 0.4	0.35 ± 0.06	0.17 ± 0.03	0.25 ± 0.02	2,3
RXJ1532.9+3021	5.5 ± 0.40	20.5 ± 0.9	0.52 ± 0.12	0.18 ± 0.02	0.07 ± 0.01	2
MACS1720.3+3536	6.6 ± 0.40	13.3 ± 0.5	0.29 ± 0.09	0.17 ± 0.02	0.57 ± 0.05	2,3
Abell 2261	7.6 ± 0.30	18.0 ± 0.2	0.31 ± 0.06	0.10 ± 0.01	0.71 ± 0.06	5
MACS1931.8-2635	6.7 ± 0.40	20.9 ± 0.6	0.26 ± 0.08	0.30 ± 0.01	0.28 ± 0.02	2,3
RXJ2129.7+0005	5.8 ± 0.40	11.4 ± 2.0	0.33 ± 0.10	0.26 ± 0.02	0.55 ± 0.05	2
MS2137-2353	5.9 ± 0.30	9.9 ± 0.3	0.41 ± 0.08	···	···	2
RXJ2248.7-4431 (Abell 1063S)	12.4 ± 0.60	69.5 ± 0.1	0.39 ± 0.06	0.20 ± 0.01	0.74 ± 0.06	6
High Magnification Clusters:						
MACS0416.1-2403	7.5 ± 0.80	16.0 ± 0.9	0.40 ± 0.14	···	···	3
MACS0647.8+7015	13.3 ± 1.80	32.5 ± 2.1	0.30 ± 0.19	0.36 ± 0.02	0.62 ± 0.06	3
MACS0717.5+3745	12.5 ± 0.70	55.8 ± 1.1	0.22 ± 0.07	0.30 ± 0.01	2.11 ± 0.18	3
MACS1149.6+2223	8.7 ± 0.90	30.2 ± 1.2	0.24 ± 0.11	0.25 ± 0.02	1.21 ± 0.10	3
MACS2129.4-0741	9.0 ± 1.20	22.6 ± 1.5	0.40 ± 0.17	0.19 ± 0.03	1.56 ± 0.14	3

References. — (1) Maughan et al. (2008); (2) Allen et al. (2008); (3) Ebeling et al. (2007); (4) Cavagnolo et al. (2008); (5) Mantz et al. (2010); (6) CLASH team selected cluster.

[a] The X-ray bolometric luminosity covers the energy range $0.1 - 100$ keV.
[b] The X-ray ellipticity, ϵ, and centroid shift, $\langle w\rangle$, values are from Maughan et al. (2008).
[c] The solar abundance reference values used here are from Anders & Grevesse (1989).

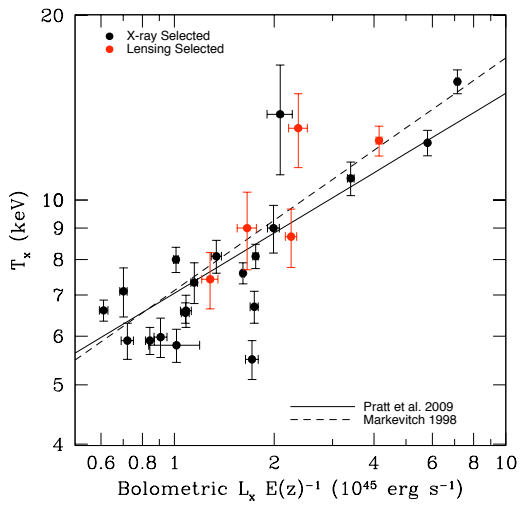

Figure 8. The X-ray temperature, T_x, as a function of the scaled bolometric luminosity, $L_x/E(z)$, for the CLASH cluster sample. Data points are from Table 4. The X-ray luminosities are scaled assuming self-similar evolution, to allow direct comparison to the low-redshift luminosity temperature relationships from Markevitch (1998) and Pratt et al. (2009). The $L_x - T_x$ relations from Markevitch (1998) and Pratt et al. (2009) (L_2 (measured within 0.15-1.00 R_{500}) vs. T_3 (0.15-0.75 R_{500})) are shown. CLASH clusters are representative of these larger X-ray cluster samples.

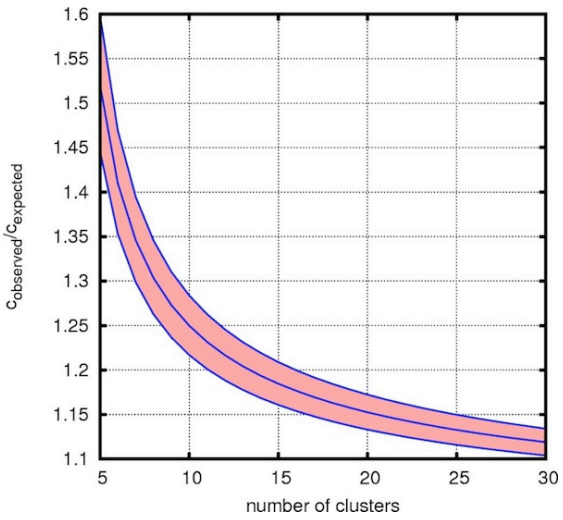

Figure 9. Mean "over-concentration" ratio necessary to reject with 99% confidence the hypothesis that measured concentrations are drawn from a sample with the expected values. Average deviations of $\sim$ 15% from expectations will be detected with 99% confidence based on our relaxed sample of 20 clusters. We have adopted the finding from ΛCDM simulations that DM halo concentrations are log-normally distributed with a standard deviation of $\sigma \approx 0.25 \pm 0.03$ (e.g., Duffy et al. 2008). The shaded band includes this uncertainty.

relaxed clusters have DM concentrations that are, on average, $\sim$ 20% higher than the general cluster population (Duffy et al. 2008; Prada et al. 2011).

- Abell 209: This system is marginally unrelaxed according to Smith et al. (2005). They based their relaxed/unrelaxed characterization mainly on a mass ratio between the cluster main component and the total mass (both at $r < 500$ kpc). Clusters with mass ratio values below 0.95 are considered unrelaxed. Their value for Abell 209 is 0.87 ± 0.06. Maughan et al. (2008), hereafter M08, derived an ellipticity of $\epsilon = 0.21 \pm 0.01$ for this cluster. Gilmour et al. (2009), hereafter G09, find it to be relaxed based on a visual examination of its X-ray morphology.

- MACSJ0329.7-0211 and CLJ1226.9+3332: these two clusters are included in the A08 compilation (as well as in Schmidt & Allen (2007), hereafter SA07, and were classified in these works as dynamically relaxed. However, M08 report that both exhibit evidence for substructure.

- MACSJ0744.9+3927: This cluster shows evidence for substructure (SA07; M08). On the other hand G09 find it to be relaxed based on a visual examination of its X-ray morphology.

- MACSJ1206.2-0848: In both optical and X-ray images the cluster appears close to relaxed in projection, with a pronounced X-ray peak at the location of the BCG. However, some evidence of merger activity along the line of sight may be suggested by the very high velocity dispersion of 1580 km s^{-1}. G09 visually classify this cluster as relaxed.

- RXJ1347.5-1145: Significant substructure is observed in this system (SA07; M08). M08 measure an average ellipticity of the X-ray isophotes of $\epsilon = 0.26 \pm 0.01$.

- Abell 2261: M08 found a small level of substructure and G09 classified it as disturbed.

- RXJ2248.7-4431: M08 found this cluster to be slightly elliptical $\epsilon = 0.2 \pm 0.01$ and with some level of substructure, while G09 found it to be relaxed.

4. SURVEY DESIGN AND IMPLEMENTATION

The CLASH program consists of 524 *HST* orbits, including 50 for supernova follow-up. The bulk of the program (474 orbits) will be used to image 25 galaxy clusters each to a depth of 20 orbits divided among 16 *HST/ACS* and *WFC3* filters as shown in Table 5 and Figure 10. The number of required cluster orbits is reduced from 500 to 474, as some of these filter depths have already been achieved in existing data. Columns 6, 7, and 8 in Table 3 provide the number of new orbits allocated, the *HST* Program ID (where available), and the number of existing archival orbits available, respectively, for each cluster. The multi-band observations span the near-ultraviolet to near-infrared (2,000 – 17,000Å). In the wavelength range $\sim$4,000–9,000Å, we use *ACS* for its greater throughput efficiency (especially toward the red end) and larger observing area.

A typical CLASH observing sequence is presented in Table 6. Each cluster is observed at two orientations to increase the area covered in the parallel field SN search. The two orientation angles are typically $\sim 30^o$ apart to minimize the overlap between the *ACS* parallel pointings (see §4.3 for more details). Although we label the visits as "A" and "B" in Table 6, either orientation may be executed first. The choice depends solely on scheduling constraints. Indeed, there are often overlaps in time

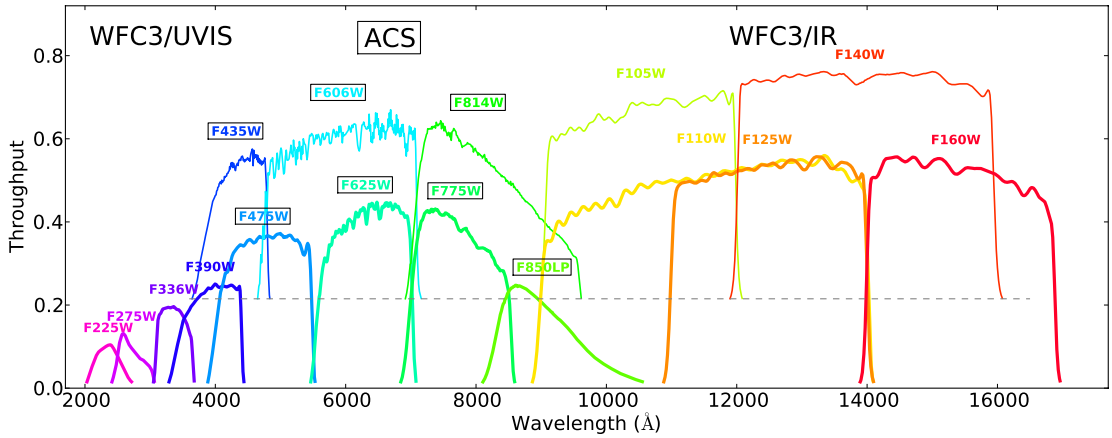

Figure 10. Each CLASH cluster is observed in 16 *HST* filters spanning ∼2,000–17,000Å with *WFC3/UVIS* in the near-ultraviolet, *ACS* in the optical (extending into the near-infrared), and *WFC3/IR* in the near-infrared (see Table 5). Total throughput curves are plotted for each filter. For clarity, some curves are offset vertically by 0.2 (dashed line).

Table 5
CLASH Exposure Times, Limiting Magnitudes, and Extinction Coefficients

Camera / Channel	Filter Element	Orbits	Average Exposure Time (sec)[a]	10σ Limit (AB mag)[b]	5σ Limit (AB mag)[b]	Galactic Ext. (AB mag/E(B-V))
WFC3/UVIS	F225W	1.5	3558	25.7	26.4	7.474
WFC3/UVIS	F275W	1.5	3653	25.7	26.5	6.140
WFC3/UVIS	F336W	1.0	2348	25.9	26.6	5.090
WFC3/UVIS	F390W	1.0	2350	26.5	27.2	4.514
ACS/WFC	F435W	1.0	1984	26.4	27.2	4.117
ACS/WFC	F475W	1.0	1994	26.8	27.6	3.724
ACS/WFC	F606W	1.0	1975	26.9	27.6	2.929
ACS/WFC	F625W	1.0	2008	26.4	27.2	2.671
ACS/WFC	F775W	1.0	2022	26.2	27.0	2.018
ACS/WFC	F814W	2.0	4103	27.0	27.7	1.822
ACS/WFC	F850LP	2.0	4045	26.0	26.7	1.473
WFC3/IR	F105W	1.0	2645	26.6	27.3	1.015
WFC3/IR	F110W	1.0	2415	27.0	27.8	0.876
WFC3/IR	F125W	1.0	2425	26.5	27.2	0.757
WFC3/IR	F140W	1.0	2342	26.7	27.4	0.609
WFC3/IR	F160W	2.0	4920	26.7	27.5	0.470

[a] Exposure times are the average time for each filter for all CLASH cycle 18 observations. Exposure times for cycles 19 and 20 may differ slightly due to scheduling considerations.
[b] Limiting magnitudes are for a circular aperture that is 0.4 arcsec in diameter.

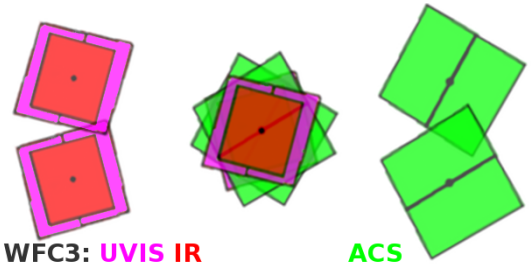

Figure 11. Each cluster is observed at two orientations approximately 30 degrees apart to increase the supernova search area in the parallel fields. *WFC3* parallel observations are obtained while the cluster core is being observed with *ACS* and vice versa. At the median cluster redshift of $z_{med} = 0.4$, the 6 arcminute separation between the center of the parallel field and the cluster center corresponds to a projected distance of 1.9 Mpc.

when the "A" and "B" orientations are both being executed. When the entire sequence of exposures for a cluster is completed, the region covered by all 16 filters subtends an area of 4.08 square arcminutes. Larger areas about the cluster center are covered by *ACS* in 7 filters. The survey footprint and exposure map are shown in Figure 11. Color images of the co-added *HST* data from the first 4 CLASH cluster are shown in Figure 12.

CLASH clusters will be observed over the course of three annual *HST* observing cycles, with 10, 10, and 5 clusters to be observed in cycles 18, 19, and 20, respectively. The current assignments of the cluster observations to the *HST* cycle number are shown in column 5 of Table 3. The duration of this MCT program is driven, in part, by the cadence required by supernova search (see §4.3 below).

4.1. *Filter Selection and Exposure Times*

Redshift estimates for multiply-lensed images are crucial for breaking lensing degeneracies and tightening constraints on mass profiles (e.g., Broadhurst et al. 2005; Zitrin et al. 2009; Saha & Read 2009). However, most of the useful lensed images are much too faint for spectroscopy. Typical lensed source magnitudes are $23 < I < 28$ (Figure 13), so that only the brightest arcs yield spectroscopic redshifts even when observed with the largest

Table 6
Typical CLASH Observing Sequence

Visit ID	Epoch[b]	Primary Camera	Primary Cluster Target Filters	Parallel Camera	Parallel Field Filters
Orientation A:					
A0, A1	1A	ACS	F625W, F850LP F475W, F775W	WFC3	F350LP, F125W, F160W
A2	1A	WFC3	F110W, F160W	ACS	F775W, F850LP
A3	2A	ACS	F606W, F814W	WFC3	F350LP, F125W, F160W
A4	2A	WFC3	F110W, F160W	ACS	F775W, F850LP
A5	3A	ACS	F435W, F814W	WFC3	F350LP, F125W, F160W
A6[a]	3A	WFC3	F225W, F390W	ACS	F775W, F850LP
A8	4A	ACS	F814W, F850LP	WFC3	F350LP, F125W, F160W
A9	4A	WFC3	F110W, F160W	ACS	F775W, F850LP
Orientation B:					
B0	1B	ACS	F625W, F850LP	WFC3	F350LP, F125W, F160W
B1	1B	WFC3	F125W, F160W	ACS	F775W, F850LP
B2	2B	ACS	F606W, F775W	WFC3	F350LP, F125W, F160W
B3[a]	2B	WFC3	F275W, F390W	ACS	F775W, F850LP
B5	3B	ACS	F435W, F814W	WFC3	F350LP, F125W, F160W
B6	3B	WFC3	F336W, F105W, F140W	ACS	F775W, F850LP
B7	4B	ACS	F475W, F850LP	WFC3	F350LP, F125W, F160W
B8	4B	WFC3	F125W, F160W	ACS	F775W, F850LP

[a] Visits A6 and B3 are each executed as a single 2-orbit visit using the same guide star acquisition. This is essential to facilitate alignment of the NUV exposures.
[b] Epochs 1A – 4A are sequential in time, as are epochs 1B – 4B. However, depending on scheduling constraints, exposures for orientation B may precede or be interlaced with those for orientation A.

ground-based facilities. With continuous sampling of the broad wavelength range from the NUV to NIR ($\sim$ 2,000–17,000 Å) that is enabled with *WFC3* and *ACS* we can now obtain very accurate photometric redshifts (photo-z's) for most of the lensed objects down to an apparent F775W AB magnitude limit of 26.

For a fixed total observing time, splitting observations into multiple (ideally overlapping) filters significantly improves photo-z precision (Benítez et al. 2009). We performed simulations to inform our filter selection and estimate our eventual photo-z precision. Galaxy magnitudes, redshifts, and SEDs (spectral energy distributions) were drawn from the UDF (Coe et al. 2006) and "re-observed" with our filter set, adding noise as appropriate given our proposed depths in each filter. Photo-z's were then re-estimated using `BPZ` (Benítez 2000; Benítez et al. 2004; Coe et al. 2006). In this simulation, we find that for 16 filters, we obtain very accurate ($\Delta z \sim 0.02(1+z)$) photo-z's for 80% of objects with F775W mag < 26. Most importantly, we find that we will be able to acquire ~ 6 times as many reliable photometric redshifts than spectroscopic redshifts for objects at $z > 1$, enabling a very substantial improvement in the number of unique constraints on the DM mass distributions (see Figure 13).

The coverage provided by the 16 *WFC3* and *ACS* filters allows the Lyman-limit feature (rest frame 912Å) to be photometrically traced to redshifts as low as $z \sim 1.5$ and Lyα to be detected out to $z \sim 10$. The inclusion of NUV photometry, for example, resolves one of the most common photo-z degeneracies between the Balmer break in $z \sim 0.2$ galaxies and the Lyman break in $z \sim 3$ galaxies (Rafelski et al. 2009).

The exposure times for the primary camera (cluster center position) are set primarily by the need to achieve 80% photometric redshift completeness down to F775W = 26 AB mag. This requires ∼18 orbits per cluster as we need to achieve a 10σ limiting AB magnitude of 26 in each filter. We augment this by two orbits per cluster to extend the NIR depth to a 10σ limiting AB mag of F160W = 26.7 and F814W = 27.0 as needed for our lensed high-z galaxy search (§2.3 and see Table 5). The limiting magnitudes in Table 5 are for a $0.4''$ diameter circular aperture and a point source with a flat F_ν spectrum. The minimum exposure in any given filter is one orbit and observations in each filter are distributed over at least four exposures to ensure robust cosmic ray rejection.

The five NIR filters provide the ability to identify $z > 7$ galaxies with high confidence. Measured colors in these filters are essential for discriminating between such high-redshift galaxies and lower-redshift highly-reddened galaxies (e.g., see Figure 14). The former are generally relatively flat in F_ν (or AB magnitudes) in the NIR while the latter generally increase in brightness as a function of wavelength. Quantitatively, the following selection criteria have proven effective: $z - J > 0.8$ (a flux decrement factor of 2.1) and $J - H < 0.5$ (Bradley et al. 2008; Zheng et al. 2009; Bradley et al. 2011). To reliably measure the above colors for high-z lensed galaxy detection, our exposures are set to reach the following AB magnitude limits: F850LP: 26.7 (5σ), F110W: 27.8 (5σ), F125W: 26.5 (10σ), and F160W 26.7 (10σ).

4.2. *Dither Pattern*

In each orbit we use a compact 4−point dither pattern that provides half-pixel sampling along both detector axes. The dither pattern serves to both improve the spatial sampling of the point spread function (PSF), especially for the *WFC3/IR* detector with its large pixel scale of 0.128 arcsec/pixel, and to help remove hot pixels and other detector imperfections that may be unaccounted for in the calibration reference files. In the first epoch of each roll angle, we use a small-scale dither pattern to preserve, as best as possible in light of signifi-

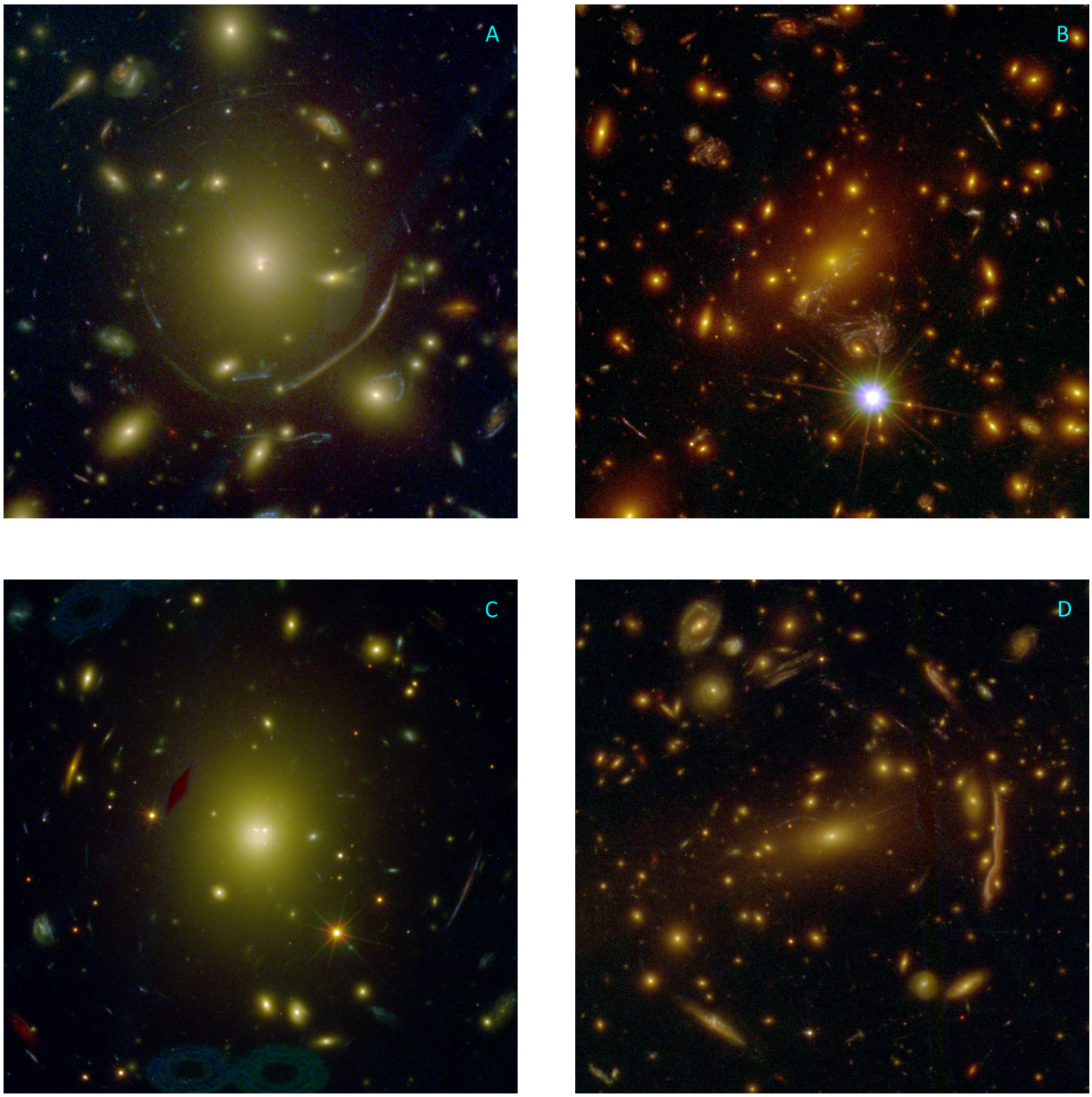

Figure 12. Cutouts of the CLASH images of the central regions of (A) Abell 383, (B) MACS1149.6+2223, (C) Abell 2261, and (D) MACS1206.2−0847. The field of view shown in each image is 65 × 65 arcseconds and is centered on the brightest cluster galaxy. These color composites are made from a combination of 12 of the 16 filters available for each cluster. The blue channel is a sum of the *ACS* F435W and F475W filters, the green channel is a sum of the *ACS* F606W, F625W, F775W, F814W, and F850LP filters, and the red channel is a sum of all five of the *WFC3/IR* broad band filters. Each cutout shown here represents ∼ 28% of the area covered by all 16 filters and just ∼ 10% of the total area imaged in the cluster core.

cant geometric distortions, half-pixel sampling across the detector. In subsequent epochs involving *WFC3/IR* observations, either in prime or parallel, we use a slightly larger dither pattern to help identify and remove persistence artifacts from compact sources, which, if uncorrected, could possibly be misidentified as SNe candidates. While our small-scale dither patterns are much smaller than is needed to cover the *WFC3/UVIS* and *ACS/WFC* detector gaps, our cluster observations are obtained at two orientations, leaving only two small diamond-shaped regions (∼ 4.4 square arcseconds each) in the central cluster area without data in all 16-filters.

4.3. *Observation Cadence and Supernova Follow-Up*

Parallel observations are being obtained with a primary science goal of detecting Type Ia SNe. While the cluster core is being imaged with *ACS*, we obtain parallels with *WFC3*, and vice versa. For each of the two roll angles, observations are obtained over the course of four epochs spread out over ∼ 30 to 45 days (∼ 10 to 14 days between observations). Image differencing analysis enables us to detect supernovae which have gone off between observations. As noted above, the exposure sequences are executed either sequentially or interleaved, depending on scheduling availability.

Upon detection of a promising high-z type Ia SN in the parallel field around a cluster, we can reprogram the remaining parallels to provide the follow-up (light curve

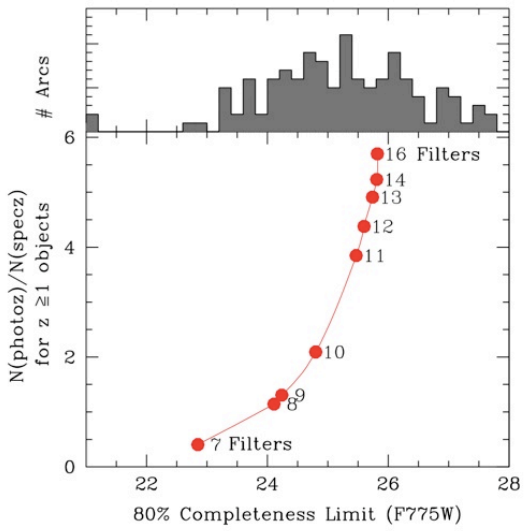

Figure 13. Top: Magnitude distribution of 132 multiply lensed images detected in A1689 and CL0024+17 (Broadhurst et al. 2005; Zitrin et al. 2009). Most are too faint for spectroscopic follow-up. Bottom: By increasing the number of filters for a fixed observing time, we show how photometric redshifts are improved using two metrics. The horizontal axis shows, for example, that 16 filters yield very accurate ($\Delta z \sim 0.02(1+z)$) photo-z's for 80% of F775W mag < 26 objects. This allows us to obtain precise redshifts for ~ 6 times more objects than attainable using spectroscopy, as shown on the vertical axis. These estimates are based on simulated photometric and photo-z catalogs derived from galaxies observed in the UDF (Coe et al. 2006).

imaging and grism spectroscopy) necessary to measure its distance. The ability to reprogram the later of the two orientations to follow-up a SN detected early in a cluster observing sequence sets the upper limit on the angular offset between the two orientations – both orientations must be accessible during the entire cluster sequence. This constraint means that the two orientations cannot be more than $\sim 30^o$ apart. A lower limit on the angular separation between the two orientations is set to $\sim 20^o$ to ensure there is not excessive overlap in the *ACS* parallel pointings (with the exception of RXJ1347 where an orientation shift of 15^o was needed to avoid placing a bright star in the parallel fields). The ability to reprogram a downstream orientation shift means that a new target of opportunity (ToO) observation will not be required if the SN is discovered early in the cluster observing sequence. In this regard, the design of the CLASH SN program has part of the follow-up built into its implementation. For the flexibility required to follow SNe found at the end of their corresponding cluster observing sequence, a small number of ToOs (four) and follow-up reserve orbits are included in the CLASH orbit allocation. CLASH parallel fields are *not* observed in 16 filters. The *ACS* parallels are taken in F775W and F850LP and the *WFC3* parallels are taken in F350LP (UVIS), F125W (IR) and F160W (IR) (see Table 6).

The CLASH and CANDELS (Grogin et al. 2011; Koekemoer et al. 2011) supernova programs are tightly coordinated and, in fact, share a common pool of reserve orbits from which both programs can draw upon for follow-up. This common reserve has been allocated 200 orbits: 50 from the CLASH allocation and 150 from CANDELS. The coordinated program is led by A. Riess who is a co-I in both programs.

4.4. *ACS Failure Options*

While *ACS* functionality was restored in SM4, it is now only a "single-string" instrument, meaning there is no redundant path if the main CCD electronics box experiences a failure. This was a constraint imposed by the nature of the *ACS* repair. The primary impact of such a failure would be the loss of our parallel observations for supernova searches. Supernovae could still be detected in our primary cluster core observations assuming we were to continue to distribute the exposures over multiple epochs. However, the use of type Ia SNe for cosmology in strongly lensed regions is fraught with difficulty (see §2.2). While a failure of *ACS* would be a significant blow to the survey's dark energy science objectives, all other components of the CLASH science program, including our prime objective of studying the distribution of mass profile properties in clusters, would be able to be pursued with *WFC3* alone.

If *ACS* fails permanently, we would abandon the dual orientation strategy and would, most likely, abandon the multiple epoch exposures, allowing the observations of each cluster to be completed on a much shorter timeframe. By observing each cluster at a single roll angle, we would slightly increase the area in which we obtain full 16-filter coverage. All of the *ACS* filters are available with *WFC3/UVIS*, which would allow us to continue our 16-filter observations with *WFC3* alone. However there would be noticeable reductions in signal-to-noise in the redder filters (F775W, F814W, F850LP). In order to continue to achieve the same depths, we would require exposure times in the redder filters to be increased by 80%, adding about four orbits of integration time to each cluster.

The *WFC3/UVIS* and *WFC3/IR* fields of view are large enough to contain and yield robust photometric redshifts for most of the strongly lensed arcs. We would lose the extra areal coverage provided by the *ACS* observations, slightly reducing the area of overlap with our Subaru images. However, we estimate the impact on our ability to measure the mass profiles over the full radial range will be negligible.

5. THE CLASH DATA PIPELINE

The bulk of our *HST* data analyses make use of mosaics of globally aligned and co-added images. To accomplish this, we use the `MosaicDrizzle` pipeline (Koekemoer et al. 2002). The `MosaicDrizzle` pipeline takes as its input the calibrated `FLT` files which have been produced by `calacs` and `calwf3`. The ACS/WFC data, however, are first corrected for bias-striping and charge-transfer efficiency (CTE) degradation effects (Anderson & Bedin 2010). The CTE correction approximately reverses the effects of charge being trapped and trailed across the image during data readout. However, a similar procedure has yet to be developed and implemented for WFC3/UVIS images. We find that this uncorrected CTE can most significantly affect our UVIS photometry as follows. Trails from cosmic rays can leak into photometric apertures of non-detections, artificially boosting their observed fluxes. Objects otherwise expected to be

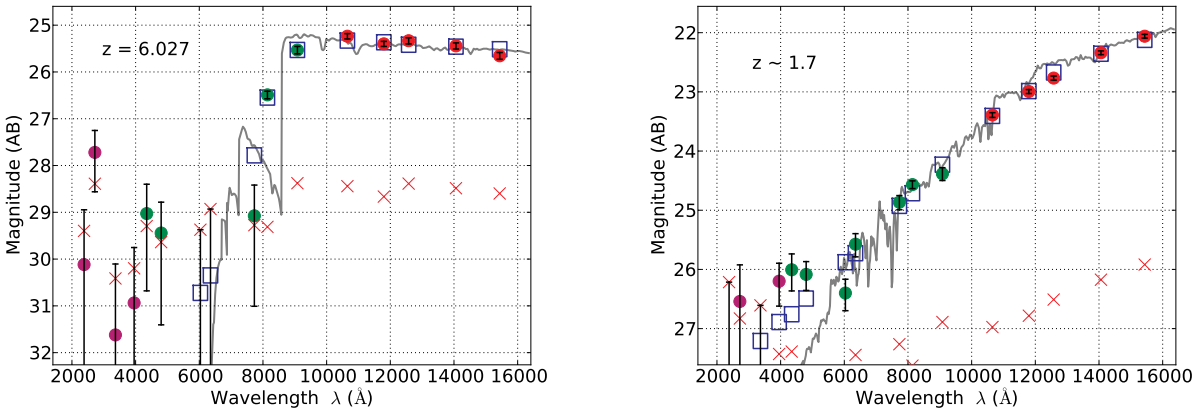

Figure 14. Robustly distinguishing between high-redshift objects (left) and lower redshift reddened galaxies (right) with the CLASH filter set. Photometry in the 16 CLASH filters is plotted versus wavelength for two galaxies behind CLASH clusters. **Left:** a spectroscopically confirmed $z = 6.027$ galaxy behind Abell 383 (Richard et al. 2011) and best fit photometric redshift $z = 6.06$. **Right:** a reddened galaxy behind Abell 2261 with photo-$z \sim 1.7$. Red X's show 1-σ detection limits based on the measured flux uncertainties, and blue boxes are SED-predicted magnitudes as integrated through each filter. Note the high redshift galaxy SED is roughly flat in the NIR, while the lower redshift SED continues to rise as a function of wavelength through the NIR. This difference, highlighted clearly in the NIR photometry, enables us to robustly distinguish high redshift galaxies from lower redshift interlopers.

UVIS dropouts, or non-detections (based on ACS+IR photometry), may commonly have significant detections in one or more UVIS filters. We find this can be greatly mitigated by adopting a more aggressive rejection of cosmic rays and their trails. The result is that most expected UVIS dropouts do actually drop out, though with some significant (as high as $\sim$ 5-σ) detections remaining.

`MosaicDrizzle` then carries out a sequence of steps aimed at aligning the exposures in all the different camera/filter combinations within each visit and also across visits, using a combination of catalog matching and cross-correlation. The catalog-matching is done using a deep ground-based catalog (typically from Subaru's Suprime Cam) as an initial reference point, followed by subsequent matching using catalogs from the CLASH *HST* images themselves, solving for shifts and rotations, which yields an accuracy of 0.1-0.2 pixel. Shifts are further refined using cross-correlation which can achieve accuracies to the level of 0.02-0.05 pixel, thus 1-2 mas for *ACS* images, limited essentially at that point by the stability of the PSF from one exposure to the next, as well as the accuracy of the distortion correction which is also removed from the images at this step.

The iterative shift refinement is then used to enable cosmic ray rejection to be carried out for all the exposures in a given filter across multiple epochs, leading to a final set of cosmic ray and bad pixel masks. These are then weighted according to the sky level in each input exposure (as modulated by the flatfield / detected quantum efficiency variation across the detector for each filter), along with the readnoise and accumulated dark current, to form an inverse variance image for each exposure. The drizzle combination is then carried out using the inverse variance images as weights, using a square kernel as well as a"pixfrac" parameter typically set to 0.8 which is chosen to be appropriate to the output image pixel scale and the number of dithers per filter. An advantage of this approach is that it involves only a single geometric operation, transforming the pixel values from the `FLT` files directly onto the output frame and avoiding any additional convolution.

It is worth noting that the inverse variance describes the expected noise in the absence of any correlated noise; in practice the images do have some amount of correlated noise (due to the PSF being sampled by the detector pixels to begin with, as well as the single-step transformation onto the output image plane), but typically this is no more than $\sim 10-15\%$ of the noise that would be expected in the absence of any correlation, and cannot be reduced further without making the output image pixels larger. For each cluster, two sets of image mosaics are generated — one drizzled to a 30 mas/pixel grid and one drizzled to a 65 mas/pixel grid (for both *ACS* and *WFC3*). We register the images with north up, and the images are aligned so that the objects are sampled by the same pixels for all the filters.

We also run a redundant image processing pipeline that is built upon the framework developed for the *ACS* GTO pipeline `APSIS` (Blakeslee et al. 2003). For the CLASH application, `APSIS` was modified to handle the *WFC3* detectors. The use of this second pipeline provides a useful verification of the photometry and astrometry as well as a redundant processing facility. The main difference between `MosaicDrizzle` and `APSIS` is that `APSIS` does not require an external astrometric reference catalog and can derive the relative image shifts from the *HST* data alone. To date, both pipelines appear to generate data of roughly similar quality with `MosaicDrizzle` producing slightly better alignment precision.

The SN detection pipeline has been developed jointly by the CLASH and CANDELS teams. It will be described in more detail in a separate paper. Briefly, the SN detection pipeline uses an image-differencing scheme to identify SN candidates. Extensive work has already been devoted to minimizing false positive detections. IR persistence is one potential source for false positives in both the SN and high-z galaxy detection projects. To address this, a dark exposure is obtained in the Earth-occultation just preceding the first visit for all CLASH and CANDELS observations. This enables a mask to be generated that can flag any suspect pixels in the initial exposure of a CLASH visit. Subsequent orbits in the visit are flagged based on our actual data.

5.1. *Object Detection and Characterization*

SExtractor (Bertin & Arnouts 1996) is used to detect objects and measure their photometry. We run SExtractor (version 2.5.0) in dual image mode, using a detection image created from a weighted sum of the *ACS/WFC* and *WFC3/IR* images. The weights come from the inverse variance images produced by `Mosaicdrizzle`. We do not use the *WFC3/UVIS* images in the construction of the detection image but, of course, run SExtractor on the *UVIS* data to compute source photometry. We also create a detection image solely from the *WFC3/IR* images to optimize the search for high redshift ($z > 6$) objects.

For object detection in the *ACS+IR* images, we require a minimum of 9 contiguous pixels at the level of the observed background RMS or higher. The detection phase background sky level is computed in 5×5 grids of cells, with each cell being 128×128 pixels. For photometry, the local sky is estimated from a 24-pixel wide rectangular annulus around each detected object. The deblender minimum contrast ratio and number of threshold levels are 0.0015 and 32, respectively. These parameters were chosen after a systematic investigation of possible values and yields reasonable performance in minimizing spurious detections and suppressing over-deblending of bright objects, while achieving reasonable completeness in detecting faint sources behind bright cluster galaxies. The segmentation map for the cluster MACS1149.6+2223 using the above parameters is shown in Figure 15.

Our image processing effectively rejects cosmic rays from the central regions of our *UVIS* and *ACS* images where we have four or more overlapping exposures. However such rejection is not possible in the corners and edges of our images, where we have fewer exposures due to our observing strategy (two roll angles and dithering). As each cosmic ray only affects a single observation, it will often only be detected in a single filter. We prune these detections from our catalog by rejecting any object with only a single 5-σ detection in one *UVIS*/*ACS* filter, as measured by SExtractor. We also reject any object without any 5-σ detections.

We perform a separate *IR*-based detection with more aggressive deblending (64 levels of 0.0001 minimum contrast) and background subtraction (3×3 grids of 64×64 pixels). This detection is slightly more sensitive to redder objects, including those at high-redshift. It also performs slightly better at deblending these fainter objects, including those at high-z as well as arcs (strongly-lensed galaxies), from brighter nearby cluster galaxies. As all *WFC3/IR* observations are obtained with multiple readouts and cosmic ray rejection, and to preserve our sensitivity to faint high-redshift objects, we do not prune this catalog based on 5-σ detections.

Automated detection of strongly lensed galaxies is often challenging due to crowding in the cluster core, especially for low-surface brightness galaxies stretched into long, thin arcs. Progress has been made (e.g., Seidel & Bartelmann 2007), and we are testing this method for use with CLASH data. Currently, manual intervention is still required for those arcs which elude detection. We compare the initial source list with arc candidates identified both visually and based on our strong lens modeling. For arcs that are either missing from the detection list or that are only partially detected, we construct manual photometric apertures. We force SExtractor to adopt these apertures using the software package SExSeg (Coe et al. 2006). Arc photometry is then derived from images in which light from the BCG has been modeled and subtracted.

Isophotal apertures are used as they have been shown to yield robust colors (Benítez et al. 2004). In the source list presented in §5.3, no aperture corrections have been applied to the magnitudes. The PSF FWHM's span $\sim$ 0.07″–0.15″ (Ford et al. 2003; Sirianni et al. 2003; Dressel 2010). The photometric corrections for PSF variation are small for extended objects for all but the faintest sources, in part because we use relatively large isophotal apertures.

Extinction corrections are derived from the Schlegel et al. (1998) IR dust emission maps, and the resulting A_λ coefficients, in AB mag per unit E(B-V), are given in Table 5. Flux uncertainties are derived by SExtractor using the inverse variance images. We have compared the flux errors so derived with the predicted uncertainties from the *ACS* and *WFC3* exposure time calculator and find excellent agreement.

5.2. *Photometric Redshifts*

We derive photometric redshift estimates using two independent packages: `BPZ` (Benítez 2000; Benítez et al. 2004; Coe et al. 2006) and `LePHARE` (Ilbert et al. 2006, hereafter `LPZ`). Both software packages use χ^2 minimization and template fitting but differ in their specific templates and their assumed priors. `LPZ` uses the SED library optimized for the COSMOS survey (Ilbert et al. 2009) without template interpolation. `BPZ` currently uses PEGASE SED templates (Fioc & Rocca-Volmerange 1997) which have been heavily recalibrated based on the FIREWORKS spectroscopic and photometric catalog Wuyts et al. (2008). `BPZ` allows for interpolation between adjacent templates and uses an empirically-derived prior on redshift and type based on observed magnitude. A full analysis of the accuracy and precision of our photometric redshift estimates will be discussed in an upcoming paper (Jouvel et al. 2012). The photoz accuracy analyses will be based on over 1,000 redshifts, obtained from the facilities described in §6.

5.3. *Source List for MACS1149.6+2223*

We present here an initial version of a representative CLASH source list for the $z = 0.544$ cluster MACS1149.6+2223. The full list is available on-line (at MAST treasury program archive website) and has over 100 parameters per object. In Table 7 we present just a small subset of the full list: 100 galaxies within 1 arcminute of the cluster center. This source list is based on the ACS+WFC3/IR detection image (see §5.1). Column 1 gives the SExtractor object ID, columns 2 and 3 give the equatorial coordinates (J2000), column 4 gives the isophotal area of the detection (in 0.065″ pixels), column 5 gives the ellipticity of the source as measured by SExtractor, column 6 gives the number of passbands in which the object is detected at a significance of 5σ or greater, and column 7 gives the total number of bands in which the object is detected. In the case of MACS1149.6+2223, there are 17 HST passbands available because the archival imaging included *ACS* F555W.

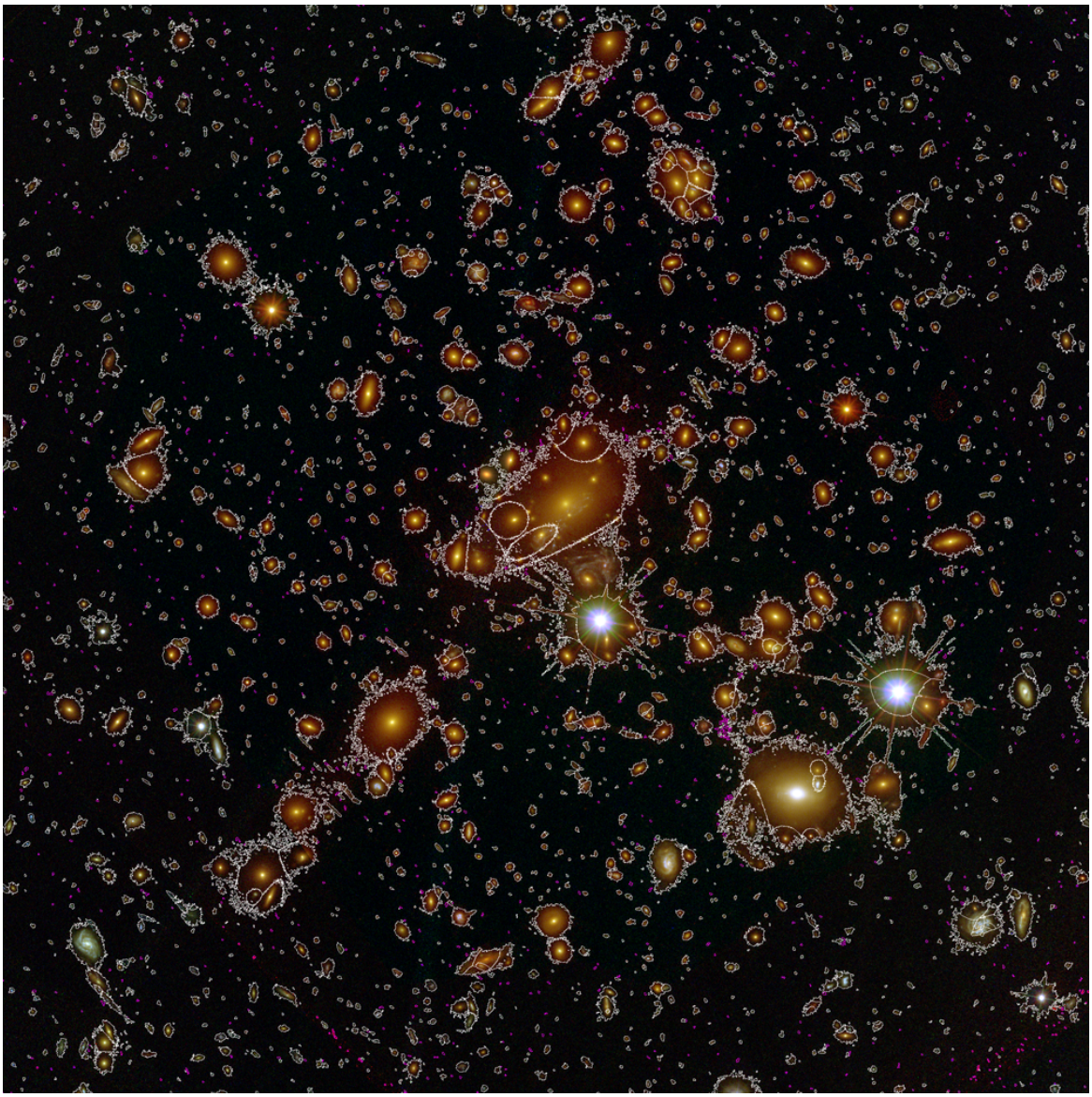

Figure 15. SExtractor segmentation map for the central region of the cluster MACS1149.6+2223. Detection of additional objects behind the cluster is accomplished by subtracting the best fits to the surface brightness distributions of the brightest of the cluster galaxies.

Note that even bright sources will sometimes not be detected in all bands because the footprints of each detector on the sky are different (see Figure 11). Columns 8 – 10 give the BPZ photometric redshift estimate, the BPZ Odds parameter (Benítez et al. 2004), and the χ^2 measurement presented in Coe et al. (2006). The 95% confidence limits on the range of the photometric redshift estimate is given in the row just below the best fit redshift value. This range is an indicator of the uncertainty in the redshift value. In general, BPZ photo-z estimates with Odds > 0.90 are the most reliable estimates. Figure 16 shows the histogram of the BPZ photometric redshifts for 232 galaxies in the cluster MACS1149.6+2223 with BPZ Odds ≥ 0.90, F850LP magnitude ≤ 26.5 and $z_{phot} \leq 3$. The histogram shows the cluster peak very clearly.

The remaining columns in Table 7 give the the isophotal magnitudes (corrected for Galactic extinction) for five of the CLASH passbands: F275W, F390W, F850LP, F125W, and F160W. The photometric error in the isophotal magnitude is given, in parentheses, in the row directly below the magnitude value. Photometry has been corrected for Galactic extinction using an E(B-V) = 0.02297 and all magnitudes given are on the AB photometric system (see Table 5 for extinction coefficients used). A magnitude value of 99 indicates a non-detection (negative flux) in that band. In this case, the magnitude error value gives the 1σ detection limit in that band. A magnitude value of -99 indicates the source lies outside of the detector field of view or lies within a gap between detectors. Source lists for each CLASH cluster are released, via MAST, ~ 6 months after the final observation for that cluster is acquired.

6. SUPPORTING OBSERVATIONS

As discussed above, having both weak and strong lensing information as well as information about the cluster baryonic mass distribution are critical for deriving robust mass profiles and concentrations. A partial list of the supporting multi-wavelength imaging being used in the

Table 7
Sample of CLASH Source List for MACS1149.6+2223

ID	α_{J2000}	δ_{J2000}	Area (Pixels)	Ell	Nsig5	Nfobs	zbpz [min,max]	odds	χ^2	F275W (err)	F390W (err)	F850LP (err)	F125W (err)	F160W (err)
4756	177.4090	22.4002	9	0.36	4	17	2.990 [2.73,3.09]	0.63	1.32	29.64 (1.50)	29.05 (0.65)	27.18 (0.22)	28.65 (0.52)	28.10 (0.30)
4761	177.3900	22.3999	65	0.47	12	17	1.701 [1.62,1.75]	0.94	2.44	26.85 (0.49)	26.73 (0.24)	26.87 (0.39)	25.42 (0.08)	25.65 (0.08)
4762	177.3900	22.4002	10	0.45	4	17	1.717 [1.49,1.77]	0.59	0.63	29.20 (1.53)	28.16 (0.48)	27.16 (0.33)	26.82 (0.17)	27.11 (0.19)
4763	177.3900	22.4000	8	0.42	1	17	0.765 [0.76,2.22]	0.12	0.63	99.00 (28.12)	28.19 (0.44)	27.28 (0.32)	27.26 (0.21)	27.36 (0.20)
4764	177.3910	22.4002	29	0.27	12	17	1.222 [1.12,1.32]	0.63	1.98	99.00 (28.01)	27.69 (0.34)	26.44 (0.18)	26.24 (0.10)	26.26 (0.09)
4765	177.4080	22.4002	15	0.16	8	17	0.745 [0.67,4.03]	0.31	1.47	99.00 (28.04)	99.00 (28.89)	26.59 (0.19)	26.94 (0.18)	26.85 (0.14)
4773	177.4140	22.4002	4	0.31	1	17	1.150 [1.25,2.41]	0.14	0.87	28.89 (0.95)	27.87 (0.25)	27.97 (0.39)	28.95 (0.60)	28.03 (0.27)
4778	177.3880	22.3999	152	0.13	12	17	0.453 [0.43,0.47]	0.98	4.00	25.34 (0.20)	26.62 (0.30)	23.78 (0.04)	23.48 (0.02)	23.30 (0.01)
4780	177.4130	22.4000	260	0.03	13	17	0.685 [0.66,0.72]	0.91	5.22	26.26 (0.53)	26.32 (0.29)	23.35 (0.03)	23.23 (0.02)	23.00 (0.01)
4782	177.3890	22.4001	8	0.06	2	17	2.344 [2.20,2.76]	0.32	0.28	99.00 (28.58)	28.35 (0.36)	28.67 (0.67)	27.85 (0.25)	27.07 (0.11)
4784	177.4100	22.4000	10	0.51	4	17	0.887 [0.51,1.00]	0.37	1.86	26.50 (0.28)	27.07 (0.22)	26.65 (0.22)	27.06 (0.23)	27.52 (0.29)
4786	177.3870	22.4001	5	0.03	2	17	3.898 [3.65,4.08]	0.64	1.30	99.00 (28.87)	30.42 (1.21)	28.65 (0.53)	29.30 (0.60)	29.74 (0.72)
4787	177.4100	22.3998	164	0.53	12	17	0.507 [0.46,0.54]	0.80	3.54	25.89 (0.34)	27.03 (0.43)	24.17 (0.06)	24.19 (0.04)	24.23 (0.04)
4788	177.4140	22.4001	7	0.20	2	17	2.472 [1.93,2.68]	0.40	0.83	99.00 (28.45)	27.85 (0.27)	27.84 (0.38)	28.24 (0.38)	28.82 (0.51)
4792	177.3820	22.4000	5	0.45	6	17	0.587 [0.45,2.98]	0.31	0.67	99.00 (27.95)	28.13 (0.49)	27.33 (0.40)	26.98 (0.20)	26.83 (0.15)
4793	177.3910	22.3998	387	0.29	14	17	3.248 [3.23,3.27]	1.00	1.93	25.38 (0.28)	25.03 (0.11)	23.05 (0.03)	23.01 (0.02)	22.69 (0.01)
4794	177.3910	22.3999	26	0.36	11	17	3.274 [3.25,3.42]	0.92	1.34	99.00 (28.36)	28.92 (0.64)	26.96 (0.20)	26.71 (0.12)	26.44 (0.08)
4799	177.3830	22.3998	115	0.21	16	17	1.140 [1.13,1.17]	1.00	2.94	25.07 (0.15)	24.97 (0.07)	24.06 (0.05)	23.98 (0.03)	23.74 (0.02)
4800	177.3840	22.3998	132	0.20	13	17	0.714 [0.67,0.74]	0.88	2.33	25.64 (0.22)	26.46 (0.23)	24.59 (0.07)	24.71 (0.05)	24.78 (0.05)
4801	177.3840	22.3997	472	0.10	15	17	0.528 [0.46,0.54]	0.82	4.85	24.30 (0.14)	24.56 (0.09)	22.75 (0.03)	22.72 (0.02)	22.63 (0.01)
4805	177.3950	22.4000	29	0.21	12	17	0.906 [0.88,0.94]	0.95	3.55	27.30 (0.49)	27.30 (0.26)	25.84 (0.12)	26.34 (0.12)	26.50 (0.12)
4806	177.4070	22.4000	58	0.34	14	17	0.776 [0.74,0.84]	0.81	2.52	26.09 (0.25)	26.48 (0.18)	25.48 (0.11)	24.99 (0.05)	24.91 (0.04)
4812	177.4150	22.3999	69	0.19	10	17	0.347 [0.30,0.39]	0.74	1.53	99.00 (27.49)	27.99 (0.61)	25.82 (0.16)	24.93 (0.05)	24.81 (0.04)
4813	177.4050	22.3998	321	0.04	14	17	0.505 [0.49,0.52]	1.00	2.09	27.06 (0.94)	25.72 (0.19)	22.59 (0.02)	22.17 (0.01)	21.85 (0.01)
4820	177.3840	22.4007	76	0.02	11	17	0.772 [0.71,0.84]	0.73	3.08	99.00 (27.36)	26.97 (0.32)	25.31 (0.12)	25.03 (0.06)	25.00 (0.05)
4821	177.3920	22.3995	76	0.11	10	17	0.742 [0.54,0.81]	0.49	2.22	27.21 (0.68)	99.00 (28.17)	25.56 (0.14)	24.99 (0.06)	24.78 (0.04)
4822	177.3920	22.3998	32	0.34	9	17	0.560 [0.34,3.09]	0.11	0.89	27.40 (0.69)	27.48 (0.41)	26.13 (0.21)	26.52 (0.19)	26.01 (0.11)
4827	177.3860	22.3998	5	0.09	1	17	0.650 [0.53,0.82]	0.40	0.71	27.72 (0.37)	28.66 (0.42)	28.34 (0.49)	28.44 (0.36)	28.33 (0.29)
4832	177.4120	22.3996	66	0.54	14	17	2.739 [2.64,2.75]	0.96	1.41	99.00 (27.56)	26.10 (0.13)	25.33 (0.10)	25.31 (0.07)	25.03 (0.05)
4841	177.4040	22.3996	74	0.37	14	17	0.371 [0.34,0.47]	0.70	5.95	26.80 (0.57)	27.16 (0.41)	24.63 (0.07)	25.42 (0.10)	25.07 (0.06)
4843	177.3890	22.3996	21	0.55	6	17	0.768 [0.64,1.03]	0.37	0.92	99.00 (27.85)	27.84 (0.42)	26.57 (0.23)	26.19 (0.11)	26.03 (0.08)
4853	177.4140	22.3994	56	0.28	13	17	2.201 [2.19,2.33]	0.82	2.38	27.57 (0.75)	25.83 (0.10)	26.66 (0.29)	25.94 (0.11)	25.27 (0.05)
4856	177.4050	22.4009	21	0.33	8	17	0.767 [0.63,0.92]	0.41	2.30	26.01 (0.20)	27.68 (0.40)	26.15 (0.17)	26.34 (0.14)	26.01 (0.09)
4868	177.4060	22.3994	21	0.17	7	17	0.558 [0.51,0.97]	0.27	1.64	27.33 (0.53)	27.98 (0.47)	26.42 (0.19)	26.68 (0.17)	26.26 (0.10)
4869	177.4060	22.3991	215	0.03	12	17	0.455 [0.43,0.47]	0.99	2.13	25.70 (0.33)	26.90 (0.44)	23.48 (0.04)	23.16 (0.02)	22.90 (0.01)

Note. — The full source list with over 100 parameters per source is available on-line from IOP and from the MAST CLASH Treasury Archive webpage at http://archive.stsci.edu/prepds/clash/

All magnitudes are on AB system.

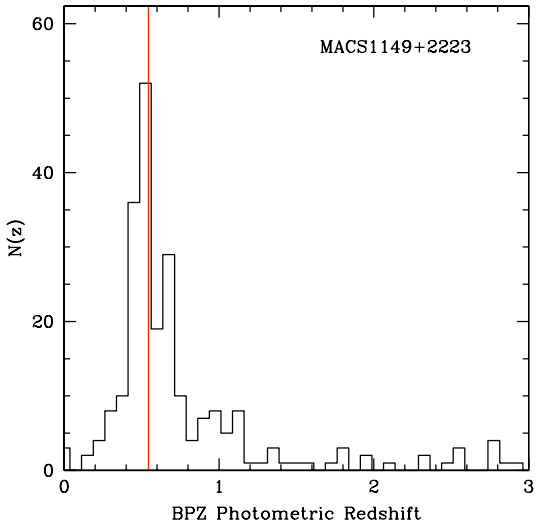

Figure 16. Histogram of the BPZ photometric redshifts for galaxies within 1 arcminute of the center of the cluster MACS1149.6+2223. The 232 galaxies included here have BPZ Odds $\geq$ 0.90, F850LP magnitude $\leq$ 26.5 and $z_{phot} \leq 3$. The histogram shows the cluster peak very clearly. The mean spectroscopic redshift of the cluster ($z = 0.544$) is denoted by the vertical red line. The average photometric redshift in the range $0.4 \leq z_{phot} \leq 0.65$ is $\langle z_{ph} \rangle = 0.515$. The accuracy of our photometric redshifts is expected to improve further as our spectroscopic sample increases. See Jouvel et al. (2012) for details.

CLASH program is summarized in Table 8. All CLASH clusters have X-ray imaging as well as wide-field multi-band ground-based optical imaging. The X-ray imaging is from Chandra/ACIS (Garmire et al. 2003) and some of the clusters have XMM/EPIC (Strüder et al. 2001; Turner et al. 2001) imaging as well.

The ground-based optical imaging is, for 24 out of the 25 clusters, from the Subaru Observatory (and, in particular, performed with the SuprimeCam instrument (Miyazaki et al. 1998)). The Subaru SuprimeCam imaging is currently available in three or more filters for 22 of the 24 clusters reachable from Mauna Kea and we are pursuing additional optical filter coverage for the two remaining clusters. Wide-field optical imaging for Abell 2261 from Subaru, for instance, was supplemented with SDSS *iz* band imaging from the Kitt Peak 4-m Mayall telescope using the Mosaic1 camera. RXJ2248.7-4431, is too far south to reach with Subaru but has multi-band imaging from the wide-field imager (WFI) on the European Southern Observatory's 2.2m telescope. The multi-band optical imaging enables robust selection of background galaxies for weak lensing analysis (e.g., Medezinski et al. 2007).

We have also acquired mm-wave imaging to map the Sunyaev-Zel'dovich Effect (SZE) in order to measure the integrated line-of-sight gas pressure towards each cluster. The SZE data come primarily from two facilities – the Bolocam instrument at the Caltech Submillimeter Observatory (Golwala et al. 2009; Sayers et al. 2011) and Multiplexed SQUID/TES Array at Ninety Gigahertz (MUSTANG; Dicker et al. 2008, 2009) at the Robert C. Byrd Green Bank Telescope. All 25 CLASH clusters have a detected SZE signal with the lowest SNR$\sim$ 7 and most with SNR > 10. The combination of the X-ray and mm-wave observations allow the mass scaling relations to be accurately calibrated for use in cosmological surveys (e.g., Okabe et al. 2010b). The X-ray and SZE data will be used to measure gas density profiles for subtraction from lensing-derived total mass profiles to yield DM-only mass profiles (e.g., Lemze et al. 2008). These data also allow assumptions of hydrostatic equilibrium to be tested and constraints on thermal motion to be made from measurements of excess pressure (Umetsu et al. 2009; Zhang et al. 2010; Molnar et al. 2010).

Spitzer Space Telescope (Werner et al. 2004) data is available for most of the CLASH clusters from the IRAC Lensing Survey (E. Egami, P.I.). The few remaining clusters that lacked sufficiently deep Spitzer data will be observed in our cycle 8 ICLASH program (R. Bouwens, P.I.). The Spitzer data are critical for characterizing the high-z galaxy population (e.g., see Richard et al. (2011)). Deep IRAC (Fazio et al. 2004) imaging samples the rest-frame optical in high-z galaxies, allowing us to perform stellar population modeling and derive stellar masses, and enables robust discrimination between star-forming $z > 7$ galaxies and dusty/evolved galaxies at $z \sim 2$.

We have also been awarded 225 hours of time on the VLT as part of a large program (P. Rosati, P.I.) to obtain VIMOS spectroscopy of the 14 southern clusters ($\delta < +1.5°$). In addition, we are acquiring cluster and lensed galaxy redshifts from spectrographs on *Magellan (GISMO; LDSS), LBT (MODS), MMT (Hectospec),* and *Palomar* (double spectrograph).

7. SUMMARY

The Cluster Lensing And Supernova survey with Hubble will produce a major advance in our understanding of the DM power spectrum and the internal structure of cluster halos on scales from 10 kpc to 2 Mpc. The precision to which these measurement are being made will provide an unprecedented foil against which we will challenge and ultimately expand our current ideas about structure formation and the nature of dark energy. In November 2010, the CLASH MCT program initiated its three year observing plan to obtain deep (20-orbit) 16-band *HST* imaging for each of 25 galaxy cluster cores. The clusters in our sample are massive ($5 \times 10^{14} < M_{vir}/M_{\odot} < 3 \times 10^{15}$), span a range of (intermediate) redshifts ($0.18 < z < 0.9$), and most (20 of the 25) were selected based on their X-ray properties (reasonably relaxed and $T_x > 5$ keV). The 16-band *HST* imaging yields precise ($2\%(1+z)$) photometric redshifts for all galaxies brighter that F775W AB mag 26, including hundreds of strongly lensed galaxies. When combined with weak lensing maps from wide field Subaru imaging and constraints on the baryonic gas distribution from mm-wave and X-ray imaging, CLASH data will allow the cluster mass profiles to be tightly constrained over a large range of scales, yielding robust measurements of their central density concentrations. We also expect to provide important constraints on the degree of substructure in the DM distribution by studying galaxy-scale lensing. The strong lens magnifying power of our clusters should also enable detection of dozens of relatively bright ($m < 26$ AB) $z > 7$ galaxies, including some bright enough for spectroscopic follow-up with ground-based telescopes and, certainly, many that can be studied with the spectrographs on *JWST*. Parallel observations

Table 8
Partial List of Supporting Observations for CLASH at Time of Publication

Cluster	Proj. FOV of Suprime Cam (Mpc)	Suprime Cam Filters	Chandra (ksec)	XMM (ksec)	Spitzer[a] (ksec)	Bolocam (ksec)
X-ray Selected Clusters:						
Abell 209	5.68	BVRIZ	20	···	(31.2)[b]	66
Abell 383	5.26	BVRIZ	50	···	20.4	91
MACS0329.7-0211	9.68	BVRZ	70	···	(31.2)[b]	39
MACS0429.6-0253	9.30	VRI	24	···	(31.2)[b]	62
MACS0744.9+3927	11.90	BVRIZ	90	138	18.0	62
Abell 611	7.28	BVRIZ	40	28	18.0	79
MACS1115.9+0129	8.34	BVRIZ	56	···	(31.2)[b]	56
Abell 1423	5.82	VI	36	31	···	TBA[d]
MACS1206.2-0847	9.56	BVRIZ	24	···	(31.2)[b]	41
CLJ1226.9+3332	13.04	BVZ	75	120	17.0	68
MACS1311.0-0310	10.20	R	85	···	(31.2)[b]	41
RXJ1347.5-1145	9.68	BVRIZ	185	36	19.2	59
MACS1423.8+2404	10.72	BVRIZ	140	···	21.4	85
RXJ1532.9+3021	8.22	BVRIZ	40	···	20.2	53
MACS1720.3+3536	8.90	BVRIZ	60	···	20.0	68
Abell 2261	6.06	BVR	35	33	22.4	46
MACS1931.8-2635	8.34	BVRIZ	114	···	(31.2)[b]	63
RXJ2129.7+0005	6.26	BVRIZ	40	···	18.2	49
MS2137-2353	7.70	BVRIZ	150	···	20.4	47
RXJ2248.7-4431 (Abell 1063S)	···	*Not accessible* See note *c*	26	···	20.4	20
High Magnification Clusters:						
MACS0416.1-2403	9.30	BRZ	16	···	(31.2)[b]	29
MACS0647.8+7015	11.10	BVRIZ	40	···	18.0	43
MACS0717.5+3745	10.76	BVRIZ	104	···	21.4	47
MACS1149.6+2223	10.72	BVRIZ	20	···	18.0	45
MACS2129.4-0741	10.96	BVRIZ	40	···	19.5	47

Note. — Observations with MUSTANG (NRAO/GBT) pending. Spectroscopic observations summarized in text.
[a] Times shown are the total for both IRAC channels 1,2 (3.6 and 4.5 microns).
[b] These 8 clusters will be observed with the indicated exposures in Spitzer cycle 8.
[c] RXJ2248.7-4431 has UBVRIZ imaging with the WFI on the 2.2-meter telescope at La Silla. Total exposure times in each band are 10-11 hours.
[d] SZE data for A1423 will be acquired in spring 2012.

may detect up to ~ 30 $z > 1$ Type Ia supernovae that, when combined with $z > 1$ SNe Ia detected by the CANDELS program, will provide new constraints on the time-dependence of w and a dramatic improvement in our understanding of SNe Ia evolution in the matter-dominated universe ($z > 1.5$).

CLASH data will also provide the mass-calibrators for the next generation of big cosmological surveys such as the Dark Energy Survey (DES), Sunayev-Zeldovich surveys (e.g., South Pole Telescope) and next generation X-ray cluster surveys. The DES will measure the evolution of the space density of clusters (among other probes) as a way to measure Dark Energy. These cluster counts tell us much about cosmological parameters through their impact on both the volume and the growth of perturbations. To do so, however, requires that the cluster mass scaling relations be well calibrated. The CLASH measurements of the enclosed mass in each cluster will be invaluable in calibrating the relation between the cluster mass and a number of observable mass proxies.

MCT programs represent a very large investment of *HST* observing time. These data are intended to be a community resource, and as such they have no proprietary period. The zero proprietary period policy also applies to our cycle 8 Spitzer observations. All *HST* and Spitzer images may be downloaded immediately after they are obtained via the MAST and IRSA archives, respectively. The CLASH collaboration is producing high-level science products that will be publicly distributed via MAST's Treasury Program archive site[26]. This paper includes the first public release of a CLASH source list for the cluster MACS1149.6+2223 as well as uniformly re-derived X-ray properties for the 25 clusters in the sample. The CLASH HLSP include co-added and mosaicked images, weight maps, inverse variance maps, high-resolution color images, and source lists. At the end of the survey we will also release the corresponding registered X-ray surface brightness images, co-added Spitzer Space Telescope images, co-added SZE data, the calibrated lensing-derived mass and source magnification maps, the source lists with all photometric redshift information, SN coordinates and their light curves and grism spectra, and the associated spectroscopic redshift catalogs. The CLASH data provide a vast legacy archive for studies of the formation and evolution of cosmic structure.

We are especially grateful to our program coordinator Beth Perrillo for her expert assistance in implementing the *HST* observations in this program. We thank Jay

[26] http://archive.stsci.edu/hst/tall.html

Anderson and Norman Grogin for providing the *ACS* CTE and bias striping correction algorithms used in our data pipeline. Finally, we are indebted to the hundreds of people who have labored many years to plan, develop, manufacture, install, repair, and calibrate the *WFC3* and *ACS* instruments as well as to all those who maintain and operate the *Hubble Space Telescope*.

The CLASH Multi-Cycle Treasury Program (GO-12065) is based on observations made with the NASA/ESA Hubble Space Telescope. The Space Telescope Science Institute is operated by the Association of Universities for Research in Astronomy, Inc. under NASA contract NAS 5-26555. ACS was developed under NASA contract NAS 5-32864.

This research is supported in part by NASA grant HST-GO-12065.01-A, the Israel Science Foundation, the Baden-Wuerttemberg Foundation, the German Science Foundation (Transregio TR 33), Spanish MICINN grant AYA2010-22111-C03-00, funding from the Junta de Andaluca Proyecto de Excelencia NBL2003, INAF contracts ASI-INAF I/009/10/0, ASI-INAF I/023/05/0, ASI-INAF I/088/06/0, PRIN INAF 2009, and PRIN INAF 2010, NSF CAREER grant AST-0847157, the UK's STFC, the Royal Society, the Wolfson Foundation, and National Science Council of Taiwan grant NSC97-2112-M-001-020-MY3. AZ acknowledges support by the John Bahcall excellence prize. LI acknowledges support from a Conicyt FONDAP/BASAL grant. PR and SS acknowledge support from the DFG cluster of excellence Origin and Structure of the Universe program.

REFERENCES

Abell, G. O. 1958, ApJS, 3, 211
Abell, G. O., Corwin, Jr., H. G., & Olowin, R. P. 1989, ApJS, 70, 1
Allen, S. W., Rapetti, D. A., Schmidt, R. W., Ebeling, H., Morris, R. G., & Fabian, A. C. 2008, MNRAS, 383, 879
Anders, E. & Grevesse, N. 1989, Geochim. Cosmochim. Acta, 53, 197
Anderson, J. & Bedin, L. R. 2010, PASP, 122, 1035
Beckwith, S. V. W., Stiavelli, M., Koekemoer, A. M., Caldwell, J. A. R., Ferguson, H. C., Hook, R., Lucas, R. A., Bergeron, L. E., Corbin, M., Jogee, S., Panagia, N., Robberto, M., Royle, P., Somerville, R. S., & Sosey, M. 2006, AJ, 132, 1729
Bell, E. F., Wolf, C., Meisenheimer, K., Rix, H.-W., Borch, A., Dye, S., Kleinheinrich, M., Wisotzki, L., et al. 2004, ApJ, 608, 752
Benítez, N. 2000, ApJ, 536, 571
Benítez, N., Ford, H., Bouwens, R., Menanteau, F., Blakeslee, J., Gronwall, C., Illingworth, G., Meurer, G., et al. 2004, ApJS, 150, 1
Benítez, N., Moles, M., Aguerri, J. A. L., Alfaro, E., Broadhurst, T., Cabrera-Caño, J., Castander, F. J., Cepa, J., et al. 2009, ApJ, 692, L5
Bertin, E. & Arnouts, S. 1996, A&AS, 117, 393
Blakeslee, J. P., Anderson, K. R., Meurer, G. R., Benítez, N., & Magee, D. 2003, in Astronomical Society of the Pacific Conference Series, Vol. 295, Astronomical Data Analysis Software and Systems XII, ed. H. E. Payne, 257–+
Bouwens, R. J., Illingworth, G. D., Blakeslee, J. P., & Franx, M. 2006, ApJ, 653, 53
Bouwens, R. J., Illingworth, G. D., Bradley, L. D., Ford, H., Franx, M., Zheng, W., Broadhurst, T., Coe, D., et al. 2009, ApJ, 690, 1764
Bouwens, R. J., Illingworth, G. D., Franx, M., & Ford, H. 2007, ApJ, 670, 928
—. 2008, ApJ, 686, 230
Bouwens, R. J., Illingworth, G. D., Oesch, P. A., Labbe, I., Trenti, M., van Dokkum, P., Franx, M., Stiavelli, M., et al. 2010, arXiv:1006.4360
Bradley, L. D., Bouwens, R. J., Ford, H. C., Illingworth, G. D., Jee, M. J., Benítez, N., Broadhurst, T. J., Franx, M., et al. 2008, ApJ, 678, 647
Bradley, L. D., Bouwens, R. J., Zitrin, A., Smit, R., Coe, D., Ford, H. C., Zheng, W., Illingworth, G. D., et al. 2011, arXiv, 1104.2035
Brandt, T. D., Tojeiro, R., Aubourg, É., Heavens, A., Jimenez, R., & Strauss, M. A. 2010, AJ, 140, 804
Brinchmann, J. & Ellis, R. S. 2000, ApJ, 536, L77
Broadhurst, T., Benítez, N., Coe, D., Sharon, K., Zekser, K., White, R., Ford, H., Bouwens, R., et al. 2005, ApJ, 621, 53
Broadhurst, T., Umetsu, K., Medezinski, E., Oguri, M., & Rephaeli, Y. 2008, ApJ, 685, L9
Broadhurst, T. J. & Barkana, R. 2008, MNRAS, 390, 1647
Bunker, A. J., Wilkins, S., Ellis, R. S., Stark, D. P., Lorenzoni, S., Chiu, K., Lacy, M., Jarvis, M. J., et al. 2010, MNRAS, 409, 855
Buote, D. A., Gastaldello, F., Humphrey, P. J., Zappacosta, L., Bullock, J. S., Brighenti, F., & Mathews, W. G. 2007, ApJ, 664, 123
Capak, P., Mobasher, B., Scoville, N. Z., McCracken, H., Ilbert, O., Salvato, M., Menéndez-Delmestre, K., Aussel, H., et al. 2011, ApJ, 730, 68
Castellano, M., Fontana, A., Paris, D., Grazian, A., Pentericci, L., Boutsia, K., Santini, P., Testa, V., et al. 2010, A&A, 524, A28+
Cavagnolo, K. W., Donahue, M., Voit, G. M., & Sun, M. 2008, ApJ, 682, 821
Clowe, D., Bradač, M., Gonzalez, A. H., Markevitch, M., Randall, S. W., Jones, C., & Zaritsky, D. 2006, ApJ, 648, L109
Coe, D. 2010, arXiv, 1005.0411
Coe, D., Benitez, N., Broadhurst, T., Moustakas, L., & Ford, H. 2010, arXiv, 1005.0398
Coe, D., Benítez, N., Sánchez, S. F., Jee, M., Bouwens, R., & Ford, H. 2006, AJ, 132, 926
Comerford, J. M. & Natarajan, P. 2007, MNRAS, 379, 190
Cowie, L. L., Hu, E. M., & Songaila, A. 1995, Nature, 377, 603
Cowie, L. L., Songaila, A., Hu, E. M., & Cohen, J. G. 1996, AJ, 112, 839
Dahlen, T., Strolger, L.-G., & Riess, A. G. 2008, ApJ, 681, 462
Dahlen, T., Strolger, L.-G., Riess, A. G., Mobasher, B., Chary, R.-R., Conselice, C. J., Ferguson, H. C., Fruchter, A. S., et al. 2004, ApJ, 613, 189
Dekel, A. & Birnboim, Y. 2006, MNRAS, 368, 2
Diaferio, A. & Geller, M. J. 1997, ApJ, 481, 633
Dicker, S. R., Korngut, P. M., Mason, B. S., Ade, P. A. R., Aguirre, J., Ames, T. J., Benford, D. J., Chen, T. C., et al. 2008, in Presented at the Society of Photo-Optical Instrumentation Engineers (SPIE) Conference, Vol. 7020, Society of Photo-Optical Instrumentation Engineers (SPIE) Conference Series
Dicker, S. R., Mason, B. S., Korngut, P. M., Cotton, W. D., Compiègne, M., Devlin, M. J., Martin, P. G., Ade, P. A. R., et al. 2009, ApJ, 705, 226
Dickey, J. M. & Lockman, F. J. 1990, ARA&A, 28, 215
Domínguez, I., Höflich, P., & Straniero, O. 2001, ApJ, 557, 279
Dressel, L. 2010, Wide Field Camera 3 Instrument Handbook, Version 3.0, Tech. rep., Baltimore: STScI [LINK]
Duffy, A. R., Schaye, J., Kay, S. T., & Dalla Vecchia, C. 2008, MNRAS, 390, L64
Duffy, A. R., Schaye, J., Kay, S. T., Dalla Vecchia, C., Battye, R. A., & Booth, C. M. 2010, arXiv, 1001.3447
Ebeling, H., Barrett, E., Donovan, D., Ma, C., Edge, A. C., & van Speybroeck, L. 2007, ApJ, 661, L33
Ebeling, H., Edge, A. C., & Henry, J. P. 2001, ApJ, 553, 668
Ebeling, H., Edge, A. C., Mantz, A., Barrett, E., Henry, J. P., Ma, C. J., & van Speybroeck, L. 2010, MNRAS, 407, 83
Einasto, J. 1965, Trudy Inst. Astroz. Alma-Ata, 51, 87
Eisenhardt, P. R. M., Brodwin, M., Gonzalez, A. H., Stanford, S. A., Stern, D., Barmby, P., Brown, M. J. I., Dawson, K., et al. 2008, ApJ, 684, 905
Elíasdóttir, Á., Limousin, M., Richard, J., Hjorth, J., Kneib, J.-P., Natarajan, P., Pedersen, K., Jullo, E., et al. 2007, arXiv, 0710.5636

Elmegreen, D. M., Elmegreen, B. G., & Hirst, A. C. 2004a, ApJ, 604, L21
Elmegreen, D. M., Elmegreen, B. G., & Sheets, C. M. 2004b, ApJ, 603, 74
Ettori, S., Gastaldello, F., Leccardi, A., Molendi, S., Rossetti, M., Buote, D., & Meneghetti, M. 2010, A&A, 524, A68+
Faber, S. M., Trager, S. C., Gonzalez, J. J., & Worthey, G. 1995, in IAU Symposium, Vol. 164, Stellar Populations, ed. P. C. van der Kruit & G. Gilmore, 249–+
Faber, S. M., Willmer, C. N. A., Wolf, C., Koo, D. C., Weiner, B. J., Newman, J. A., Im, M., Coil, A. L., et al. 2007, ApJ, 665, 265
Fazio, G. G., Hora, J. L., Allen, L. E., Ashby, M. L. N., Barmby, P., Deutsch, L. K., Huang, J.-S., Kleiner, S., Marengo, M., Megeath, S. T., Melnick, G. J., Pahre, M. A., Patten, B. M., Polizotti, J., Smith, H. A., Taylor, R. S., Wang, Z., Willner, S. P., Hoffmann, W. F., Pipher, J. L., Forrest, W. J., McMurty, C. W., McCreight, C. R., McKelvey, M. E., McMurray, R. E., Koch, D. G., Moseley, S. H., Arendt, R. G., Mentzell, J. E., Marx, C. T., Losch, P., Mayman, P., Eichhorn, W., Krebs, D., Jhabvala, M., Gezari, D. Y., Fixsen, D. J., Flores, J., Shakoorzadeh, K., Jungo, R., Hakun, C., Workman, L., Karpati, G., Kichak, R., Whitley, R., Mann, S., Tollestrup, E. V., Eisenhardt, P., Stern, D., Gorjian, V., Bhattacharya, B., Carey, S., Nelson, B. O., Glaccum, W. J., Lacy, M., Lowrance, P. J., Laine, S., Reach, W. T., Stauffer, J. A., Surace, J. A., Wilson, G., Wright, E. L., Hoffman, A., Domingo, G., & Cohen, M. 2004, ApJS, 154, 10
Fedeli, C. & Bartelmann, M. 2007, A&A, 461, 49
Fioc, M. & Rocca-Volmerange, B. 1997, A&A, 326, 950
Foley, R. J., Andersson, K., Bazin, G., de Haan, T., Ruel, J., Ade, P. A. R., Aird, K. A., Armstrong, R., et al. 2011, ApJ, 731, 86
Ford, H. C., Clampin, M., Hartig, G. F., Illingworth, G. D., Sirianni, M., Martel, A. R., Meurer, G. R., McCann, W. J., et al. 2003, in Presented at the Society of Photo-Optical Instrumentation Engineers (SPIE) Conference, Vol. 4854, Future EUV/UV and Visible Space Astrophysics Missions and Instrumentation. Edited by J. Chris Blades, Oswald H. W. Siegmund. Proceedings of the SPIE, Volume 4854, pp. 81-94 (2003)., ed. J. C. Blades, 81–94
Francis, M. J., Lewis, G. F., & Linder, E. V. 2009, MNRAS, 394, 605
Garmire, G. P., Bautz, M. W., Ford, P. G., Nousek, J. A., & Ricker, Jr., G. R. 2003, in Presented at the Society of Photo-Optical Instrumentation Engineers (SPIE) Conference, Vol. 4851, Society of Photo-Optical Instrumentation Engineers (SPIE) Conference Series, ed. J. E. Truemper & H. D. Tananbaum, 28–44
Genzel, R., Newman, S., Jones, T., Förster Schreiber, N. M., Shapiro, K., Genel, S., Lilly, S. J., Renzini, A., et al. 2010, arXiv, 1011.5360
Giavalisco, M., Ferguson, H. C., Koekemoer, A. M., Dickinson, M., Alexander, D. M., Bauer, F. E., Bergeron, J., Biagetti, C., et al. 2004, ApJ, 600, L93
Gilmour, R., Best, P., & Almaini, O. 2009, MNRAS, 392, 1509
Gobat, R., Daddi, E., Onodera, M., Finoguenov, A., Renzini, A., Arimoto, N., Bouwens, R., Brusa, M., et al. 2011, A&A, 526, A133+
Golwala, S., Ameglio, S., Pierpaoli, E., & Sayers, J. 2009, in Astronomical Society of the Pacific Conference Series, Vol. 417, Submillimeter Astrophysics and Technology: a Symposium Honoring Thomas G. Phillips, ed. D. C. Lis, J. E. Vaillancourt, P. F. Goldsmith, T. A. Bell, N. Z. Scoville, & J. Zmuidzinas, 311–+
Graur, O., Poznanski, D., Maoz, D., Yasuda, N., Totani, T., Fukugita, M., Filippenko, A. V., Foley, R. J., Silverman, J. M., Gal-Yam, A., Horesh, A., & Jannuzi, B. T. 2011, MNRAS, 417, 916
Grogin, N. A., Kocevski, D. D., Faber, S. M., Ferguson, H. C., Koekemoer, A. M., Riess, A. G., Acquaviva, V., Alexander, D. M., et al. 2011, arXiv, 1105.3753
Grossi, M. & Springel, V. 2009, MNRAS, 394, 1559
Guzman, R., Gallego, J., Koo, D. C., Phillips, A. C., Lowenthal, J. D., Faber, S. M., Illingworth, G. D., & Vogt, N. P. 1997, ApJ, 489, 559
Hennawi, J. F., Dalal, N., Bode, P., & Ostriker, J. P. 2007, ApJ, 654, 714
Hoekstra, H., Yee, H. K. C., & Gladders, M. D. 2002, ApJ, 577, 595
Horiuchi, S. & Beacom, J. F. 2010, ApJ, 723, 329
Huang, X., Morokuma, T., Fakhouri, H. K., Aldering, G., Amanullah, R., Barbary, K., Brodwin, M., Connolly, N. V., et al. 2009, ApJ, 707, L12
Iben, Jr., I. & Tutukov, A. V. 1984, ApJS, 54, 335
Ilbert, O., Arnouts, S., McCracken, H. J., Bolzonella, M., Bertin, E., Le Fèvre, O., Mellier, Y., Zamorani, G., et al. 2006, A&A, 457, 841
Ilbert, O., Capak, P., Salvato, M., Aussel, H., McCracken, H. J., Sanders, D. B., Scoville, N., Kartaltepe, J., et al. 2009, ApJ, 690, 1236
Iye, M., Ota, K., Kashikawa, N., Furusawa, H., Hashimoto, T., Hattori, T., Matsuda, Y., Morokuma, T., et al. 2006, Nature, 443, 186
Jee, M. J., Dawson, K. S., Hoekstra, H., Perlmutter, S., Rosati, P., Brodwin, M., Suzuki, N., Koester, B., et al. 2011, arXiv, 1105.3186
Jee, M. J., Ford, H. C., Illingworth, G. D., White, R. L., Broadhurst, T. J., Coe, D. A., Meurer, G. R., van der Wel, A., et al. 2007, ApJ, 661, 728
Jee, M. J., Rosati, P., Ford, H. C., Dawson, K. S., Lidman, C., Perlmutter, S., Demarco, R., Strazzullo, V., et al. 2009, ApJ, 704, 672
Johnston, D. E., Sheldon, E. S., Wechsler, R. H., Rozo, E., Koester, B. P., Frieman, J. A., McKay, T. A., Evrard, A. E., et al. 2007, arXiv, 0709.1159
Jouvel, S. et al. 2012, in prep.
Juneau, S., Glazebrook, K., Crampton, D., McCarthy, P. J., Savaglio, S., Abraham, R., Carlberg, R. G., Chen, H.-W., et al. 2005, ApJ, 619, L135
Kereš, D., Katz, N., Weinberg, D. H., & Davé, R. 2005, MNRAS, 363, 2
Khochfar, S. & Burkert, A. 2003, ApJ, 597, L117
Kimble, R. A., MacKenty, J. W., O'Connell, R. W., & Townsend, J. A. 2008, in Society of Photo-Optical Instrumentation Engineers (SPIE) Conference Series, Vol. 7010, Society of Photo-Optical Instrumentation Engineers (SPIE) Conference Series
King, L. & Mead, J. 2011, arXiv, 1105.3155
Kneib, J., Ellis, R. S., Santos, M. R., & Richard, J. 2004, ApJ, 607, 697
Koekemoer, A. M., Faber, S. M., Ferguson, H. C., Grogin, N. A., Kocevski, D. D., Koo, D. C., Lai, K., Lotz, J. M., et al. 2011, arXiv, 1105.3754
Koekemoer, A. M., Fruchter, A. S., Hook, R. N., & Hack, W. 2002, in The 2002 HST Calibration Workshop : Hubble after the Installation of the ACS and the NICMOS Cooling System, ed. S. Arribas, A. Koekemoer, & B. Whitmore, 337–+
Komatsu, E., Smith, K. M., Dunkley, J., Bennett, C. L., Gold, B., Hinshaw, G., Jarosik, N., Larson, D., et al. 2010, arXiv, 1001.4538
Kriek, M., van Dokkum, P. G., Labbé, I., Franx, M., Illingworth, G. D., Marchesini, D., & Quadri, R. F. 2009, ApJ, 700, 221
Lehnert, M. D., Nesvadba, N. P. H., Cuby, J.-G., Swinbank, A. M., Morris, S., Clément, B., Evans, C. J., Bremer, M. N., et al. 2010, Nature, 467, 940
Lemze, D., Barkana, R., Broadhurst, T. J., & Rephaeli, Y. 2008, MNRAS, 386, 1092
Lemze, D., Sadeh, S., & Rephaeli, Y. 2009, MNRAS, 397, 1876
Limousin, M., Richard, J., Jullo, E., Kneib, J.-P., Fort, B., Soucail, G., Elíasdóttir, Á., Natarajan, P., et al. 2007, ApJ, 668, 643
Limousin, M., Richard, J., Kneib, J.-P., Brink, H., Pelló, R., Jullo, E., Tu, H., Sommer-Larsen, J., et al. 2008, A&A, 489, 23
Longhetti, M., Saracco, P., Severgnini, P., Della Ceca, R., Mannucci, F., Bender, R., Drory, N., Feulner, G., et al. 2007, MNRAS, 374, 614
Macciò, A. V., Dutton, A. A., & van den Bosch, F. C. 2008, MNRAS, 391, 1940
Maizy, A., Richard, J., de Leo, M. A., Pelló, R., & Kneib, J. P. 2010, A&A, 509, A105+
Mandelbaum, R., Seljak, U., & Hirata, C. M. 2008, Journal of Cosmology and Astro-Particle Physics, 8, 6

Mannucci, F., Della Valle, M., & Panagia, N. 2006, MNRAS, 370, 773
Mantz, A., Allen, S. W., Rapetti, D., & Ebeling, H. 2010, MNRAS, 406, 1759
Maoz, D. & Badenes, C. 2010, MNRAS, 407, 1314
Maoz, D., Mannucci, F., Li, W., Filippenko, A. V., Valle, M. D., & Panagia, N. 2011, MNRAS, 412, 1508
Maoz, D., Sharon, K., & Gal-Yam, A. 2010, ApJ, 722, 1879
Markevitch, M. 1998, ApJ, 504, 27
Maughan, B. J., Jones, C., Forman, W., & Van Speybroeck, L. 2008, ApJS, 174, 117
McLure, R. J., Dunlop, J. S., Cirasuolo, M., Koekemoer, A. M., Sabbi, E., Stark, D. P., Targett, T. A., & Ellis, R. S. 2010, MNRAS, 403, 960
Mead, J. M. G., King, L. J., Sijacki, D., Leonard, A., Puchwein, E., & McCarthy, I. G. 2010, MNRAS, 406, 434
Medezinski, E., Broadhurst, T., Umetsu, K., Coe, D., Benítez, N., Ford, H., Rephaeli, Y., Arimoto, N., et al. 2007, ApJ, 663, 717
Medezinski, E., Broadhurst, T., Umetsu, K., Oguri, M., Rephaeli, Y., & Benítez, N. 2010, MNRAS, 405, 257
Meneghetti, M., Fedeli, C., Pace, F., Gottlöber, S., & Yepes, G. 2010a, A&A, 519, A90+
Meneghetti, M., Fedeli, C., Zitrin, A., Bartelmann, M., Broadhurst, T., Gottlöber, S., Moscardini, L., & Yepes, G. 2011, A&A, 530, A17+
Meneghetti, M., Rasia, E., Merten, J., Bellagamba, F., Ettori, S., Mazzotta, P., Dolag, K., & Marri, S. 2010b, A&A, 514, A93+
Miralda-Escude, J. 1998, ApJ, 501, 15
Miyazaki, S., Sekiguchi, M., Imi, K., Okada, N., Nakata, F., & Komiyama, Y. 1998, in Presented at the Society of Photo-Optical Instrumentation Engineers (SPIE) Conference, Vol. 3355, Society of Photo-Optical Instrumentation Engineers (SPIE) Conference Series, ed. S. D'Odorico, 363–374
Molnar, S. M., Chiu, I., Umetsu, K., Chen, P., Hearn, N., Broadhurst, T., Bryan, G., & Shang, C. 2010, ApJ, 724, L1
Morandi, A., Pedersen, K., & Limousin, M. 2010, arXiv, 1001.1656
Navarro, J. F., Frenk, C. S., & White, S. D. M. 1996, ApJ, 462, 563
—. 1997, ApJ, 490, 493
Navarro, J. F., Hayashi, E., Power, C., Jenkins, A. R., Frenk, C. S., White, S. D. M., Springel, V., Stadel, J., et al. 2004, MNRAS, 349, 1039
Navarro, J. F., Ludlow, A., Springel, V., Wang, J., Vogelsberger, M., White, S. D. M., Jenkins, A., Frenk, C. S., et al. 2010, MNRAS, 402, 21
Neto, A. F., Gao, L., Bett, P., Cole, S., Navarro, J. F., Frenk, C. S., White, S. D. M., Springel, V., et al. 2007, MNRAS, 381, 1450
Newman, A. B., Treu, T., Ellis, R. S., & Sand, D. J. 2011, ApJ, 728, L39+
Newman, A. B., Treu, T., Ellis, R. S., Sand, D. J., Richard, J., Marshall, P. J., Capak, P., & Miyazaki, S. 2009, ApJ, 706, 1078
Nomoto, K. 1982, ApJ, 253, 798
Oesch, P. A., Bouwens, R. J., Carollo, C. M., Illingworth, G. D., Trenti, M., Stiavelli, M., Magee, D., Labbé, I., et al. 2010a, ApJ, 709, L21
Oesch, P. A., Bouwens, R. J., Illingworth, G. D., Carollo, C. M., Franx, M., Labbé, I., Magee, D., Stiavelli, M., et al. 2010b, ApJ, 709, L16
Oguri, M. & Blandford, R. D. 2009, MNRAS, 392, 930
Oguri, M. & Hamana, T. 2011, MNRAS, 414, 1851
Oguri, M., Hennawi, J. F., Gladders, M. D., Dahle, H., Natarajan, P., Dalal, N., Koester, B. P., Sharon, K., et al. 2009, ApJ, 699, 1038
Okabe, N., Takada, M., Umetsu, K., Futamase, T., & Smith, G. P. 2010a, PASJ, 62, 811
Okabe, N., Zhang, Y., Finoguenov, A., Takada, M., Smith, G. P., Umetsu, K., & Futamase, T. 2010b, ApJ, 721, 875
Oke, J. B. 1974, ApJS, 27, 21
Ono, Y., Ouchi, M., Mobasher, B., Dickinson, M., Penner, K., Shimasaku, K., Weiner, B. J., Kartaltepe, J. S., Nakajima, K., Nayyeri, H., Stern, D., Kashikawa, N., & Spinrad, H. 2012, ApJ, 744, 83
Oser, L., Ostriker, J. P., Naab, T., Johansson, P. H., & Burkert, A. 2010, ApJ, 725, 2312
Papovich, C., Momcheva, I., Willmer, C. N. A., Finkelstein, K. D., Finkelstein, S. L., Tran, K., Brodwin, M., Dunlop, J. S., et al. 2010, ApJ, 716, 1503
Perlmutter, S., Aldering, G., Goldhaber, G., Knop, R. A., Nugent, P., Castro, P. G., Deustua, S., Fabbro, S., et al. 1999, ApJ, 517, 565
Prada, F., Klypin, A. A., Cuesta, A. J., Betancort-Rijo, J. E., & Primack, J. 2011, arXiv, 1104.5130
Pratt, G. W., Croston, J. H., Arnaud, M., & Böhringer, H. 2009, A&A, 498, 361
Pritchet, C. J., Howell, D. A., & Sullivan, M. 2008, ApJ, 683, L25
Proctor, R. N. & Sansom, A. E. 2002, MNRAS, 333, 517
Rafelski, M., Wolfe, A. M., Cooke, J., Chen, H., Armandroff, T. E., & Wirth, G. D. 2009, ApJ, 703, 2033
Richard, J., Kneib, J., Ebeling, H., Stark, D., Egami, E., & Fiedler, A. K. 2011, arXiv, 1102.5092
Richard, J., Smith, G. P., Kneib, J., Ellis, R. S., Sanderson, A. J. R., Pei, L., Targett, T. A., Sand, D. J., et al. 2010, MNRAS, 404, 325
Riess, A. G., Filippenko, A. V., Challis, P., Clocchiatti, A., Diercks, A., Garnavich, P. M., Gilliland, R. L., Hogan, C. J., et al. 1998, AJ, 116, 1009
Riess, A. G. & Livio, M. 2006, ApJ, 648, 884
Riess, A. G., Macri, L., Casertano, S., Lampeitl, H., Ferguson, H. C., Filippenko, A. V., Jha, S. W., Li, W., et al. 2011, ApJ, 730, 119
Riess, A. G., Strolger, L., Casertano, S., Ferguson, H. C., Mobasher, B., Gold, B., Challis, P. J., Filippenko, A. V., et al. 2007, ApJ, 659, 98
Riess, A. G., Strolger, L.-G., Tonry, J., Casertano, S., Ferguson, H. C., Mobasher, B., Challis, P., Filippenko, A. V., et al. 2004, ApJ, 607, 665
Rines, K. & Diaferio, A. 2006, AJ, 132, 1275
Rines, K., Geller, M. J., & Diaferio, A. 2010, ApJ, 715, L180
Rodney, S., Riess, A., Dahlen, T., Strolger, L.-G., Ferguson, H. C., Hjorth, J., et al. 2011, arXiv
Rosati, P., Tozzi, P., Gobat, R., Santos, J. S., Nonino, M., Demarco, R., Lidman, C., Mullis, C. R., et al. 2009, A&A, 508, 583
Sadeh, S. & Rephaeli, Y. 2008, MNRAS, 388, 1759
Saha, P. & Read, J. I. 2009, ApJ, 690, 154
Salvaterra, R., Della Valle, M., Campana, S., Chincarini, G., Covino, S., D'Avanzo, P., Fernández-Soto, A., Guidorzi, C., Mannucci, F., Margutti, R., Thöne, C. C., Antonelli, L. A., Barthelmy, S. D., de Pasquale, M., D'Elia, V., Fiore, F., Fugazza, D., Hunt, L. K., Maiorano, E., Marinoni, S., Marshall, F. E., Molinari, E., Nousek, J., Pian, E., Racusin, J. L., Stella, L., Amati, L., Andreuzzi, G., Cusumano, G., Fenimore, E. E., Ferrero, P., Giommi, P., Guetta, D., Holland, S. T., Hurley, K., Israel, G. L., Mao, J., Markwardt, C. B., Masetti, N., Pagani, C., Palazzi, E., Palmer, D. M., Piranomonte, S., Tagliaferri, G., & Testa, V. 2009, Nature, 461, 1258
Sand, D. J., Treu, T., Ellis, R. S., Smith, G. P., & Kneib, J. 2008, ApJ, 674, 711
Sand, D. J., Treu, T., Smith, G. P., & Ellis, R. S. 2004, ApJ, 604, 88
Sayers, J., Golwala, S. R., Ameglio, S., & Pierpaoli, E. 2011, ApJ, 728, 39
Schenker, M. A., Stark, D. P., Ellis, R. S., Robertson, B. E., Dunlop, J. S., McLure, R. J., Kneib, J.-P., & Richard, J. 2012, ApJ, 744, 179
Schlegel, D. J., Finkbeiner, D. P., & Davis, M. 1998, ApJ, 500, 525
Schmidt, R. W. & Allen, S. W. 2007, MNRAS, 379, 209
Schwope, A. D., Lamer, G., de Hoon, A., Kohnert, J., Böhringer, H., Dietrich, J. P., Fassbender, R., Mohr, J., et al. 2010, A&A, 513, L10+
Seidel, G. & Bartelmann, M. 2007, A&A, 472, 341
Sereno, M., Jetzer, P., & Lubini, M. 2010, MNRAS, 403, 2077
Sérsic, J. L. 1963, Boletin de la Asociacion Argentina de Astronomia La Plata Argentina, 6, 41
Sirianni, M., De Marchi, G., Gilliland, R., Jee, M. K., Mack, J., Ford, H. C., Illingworth, G. D., Clampin, M., et al. 2003, in Bulletin of the American Astronomical Society, Vol. 35, Bulletin of the American Astronomical Society, 722–+
Smith, G. P., Kneib, J.-P., Smail, I., Mazzotta, P., Ebeling, H., & Czoske, O. 2005, MNRAS, 359, 417

Stanford, S. A., Romer, A. K., Sabirli, K., Davidson, M., Hilton, M., Viana, P. T. P., Collins, C. A., Kay, S. T., et al. 2006, ApJ, 646, L13
Strüder, L., Briel, U., Dennerl, K., Hartmann, R., Kendziorra, E., Meidinger, N., Pfeffermann, E., Reppin, C., Aschenbach, B., Bornemann, W., Bräuninger, H., Burkert, W., Elender, M., Freyberg, M., Haberl, F., Hartner, G., Heuschmann, F., Hippmann, H., Kastelic, E., Kemmer, S., Kettenring, G., Kink, W., Krause, N., Müller, S., Oppitz, A., Pietsch, W., Popp, M., Predehl, P., Read, A., Stephan, K. H., Stötter, D., Trümper, J., Holl, P., Kemmer, J., Soltau, H., Stötter, R., Weber, U., Weichert, U., von Zanthier, C., Carathanassis, D., Lutz, G., Richter, R. H., Solc, P., Böttcher, H., Kuster, M., Staubert, R., Abbey, A., Holland, A., Turner, M., Balasini, M., Bignami, G. F., La Palombara, N., Villa, G., Buttler, W., Gianini, F., Lainé, R., Lumb, D., & Dhez, P. 2001, A&A, 365, L18
Su, J., Stiavelli, M., Oesch, P., Trenti, M., Bergeron, E., Bradley, L., Carollo, M., Dahlen, T., Ferguson, H. C., Giavalisco, M., Koekemoer, A., Lilly, S., Lucas, R. A., Mobasher, B., Panagia, N., & Pavlovsky, C. 2011, ApJ, 738, 123
Tanvir, N. R., Fox, D. B., Levan, A. J., Berger, E., Wiersema, K., Fynbo, J. P. U., Cucchiara, A., Krühler, T., et al. 2009, Nature, 461, 1254
Thomas, D., Maraston, C., Bender, R., & Mendes de Oliveira, C. 2005, ApJ, 621, 673
Totani, T., Morokuma, T., Oda, T., Doi, M., & Yasuda, N. 2008, PASJ, 60, 1327
Trujillo, I., Feulner, G., Goranova, Y., Hopp, U., Longhetti, M., Saracco, P., Bender, R., Braito, V., et al. 2006, MNRAS, 373, L36
Turner, M. J. L., Abbey, A., Arnaud, M., Balasini, M., Barbera, M., Belsole, E., Bennie, P. J., Bernard, J. P., Bignami, G. F., Boer, M., Briel, U., Butler, I., Cara, C., Chabaud, C., Cole, R., Collura, A., Conte, M., Cros, A., Denby, M., Dhez, P., Di Coco, G., Dowson, J., Ferrando, P., Ghizzardi, S., Gianotti, F., Goodall, C. V., Gretton, L., Griffiths, R. G., Hainaut, O., Hochedez, J. F., Holland, A. D., Jourdain, E., Kendziorra, E., Lagostina, A., Laine, R., La Palombara, N., Lortholary, M., Lumb, D., Marty, P., Molendi, S., Pigot, C., Poindron, E., Pounds, K. A., Reeves, J. N., Reppin, C., Rothenflug, R., Salvetat, P., Sauvageot, J. L., Schmitt, D., Sembay, S., Short, A. D. T., Spragg, J., Stephen, J., Strüder, L., Tiengo, A., Trifoglio, M., Trümper, J., Vercellone, S., Vigroux, L., Villa, G., Ward, M. J., Whitehead, S., & Zonca, E. 2001, A&A, 365, L27
Umetsu, K., Birkinshaw, M., Liu, G., Wu, J., Medezinski, E., Broadhurst, T., Lemze, D., Zitrin, A., et al. 2009, ApJ, 694, 1643
Umetsu, K., Broadhurst, T., Zitrin, A., Medezinski, E., Coe, D., & Postman, M. 2011a, arXiv, 1105.0444
Umetsu, K., Broadhurst, T., Zitrin, A., Medezinski, E., & Hsu, L. 2011b, ApJ, 729, 127
Umetsu, K., Medezinski, E., Broadhurst, T., Zitrin, A., Okabe, N., Hsieh, B., & Molnar, S. M. 2010, ApJ, 714, 1470
van den Bergh, S. 1996, AJ, 112, 2634
van Dokkum, P. G. 2008, ApJ, 674, 29
Webbink, R. F. 1984, ApJ, 277, 355
Werner, M. W., Roellig, T. L., Low, F. J., Rieke, G. H., Rieke, M., Hoffmann, W. F., Young, E., Houck, J. R., Brandl, B., Fazio, G. G., Hora, J. L., Gehrz, R. D., Helou, G., Soifer, B. T., Stauffer, J., Keene, J., Eisenhardt, P., Gallagher, D., Gautier, T. N., Irace, W., Lawrence, C. R., Simmons, L., Van Cleve, J. E., Jura, M., Wright, E. L., & Cruikshank, D. P. 2004, ApJS, 154, 1
Whelan, J. & Iben, Jr., I. 1973, ApJ, 186, 1007
Worthey, G. 1996, in Astronomical Society of the Pacific Conference Series, Vol. 98, From Stars to Galaxies: the Impact of Stellar Physics on Galaxy Evolution, ed. C. Leitherer, U. Fritze-von-Alvensleben, & J. Huchra, 467–+
Wuyts, S., Labbé, I., Schreiber, N. M. F., Franx, M., Rudnick, G., Brammer, G. B., & van Dokkum, P. G. 2008, ApJ, 682, 985
Zhang, Y., Okabe, N., Finoguenov, A., Smith, G. P., Piffaretti, R., Valdarnini, R., Babul, A., Evrard, A. E., et al. 2010, ApJ, 711, 1033
Zheng, W., Bradley, L. D., Bouwens, R. J., Ford, H. C., Illingworth, G. D., Benítez, N., Broadhurst, T., Frye, B., et al. 2009, ApJ, 697, 1907
Zitrin, A., Broadhurst, T., Barkana, R., Rephaeli, Y., & Benítez, N. 2011a, MNRAS, 410, 1939
Zitrin, A., Broadhurst, T., Bartelmann, M., Rephaeli, Y., Oguri, M., Benítez, N., Hao, J., & Umetsu, K. 2011b, arXiv, 1105.2295
Zitrin, A., Broadhurst, T., Coe, D., Liesenborgs, J., Benítez, N., Rephaeli, Y., Ford, H., & Umetsu, K. 2011c, MNRAS, 413, 1753
Zitrin, A., Broadhurst, T., Umetsu, K., Coe, D., Benítez, N., Ascaso, B., Bradley, L., Ford, H., et al. 2009, MNRAS, 396, 1985
Zitrin, A., Broadhurst, T., Umetsu, K., Rephaeli, Y., Medezinski, E., Bradley, L., Jiménez-Teja, Y., Benítez, N., et al. 2010, MNRAS, 408, 1916